The Thesis Committee for Jaime Martinez
certifies that this is the approved version of the following thesis:

Large Eddy Simulation Analysis of Non-Reacting Sprays Inside a High-G Combustor

APPROVED BY

SUPERVISING COMMITTEE:

Venkatramanan Raman, Supervisor

Noel T. Clemens

Large Eddy Simulation Analysis of Non-Reacting Sprays Inside a High-G Combustor

by

Jaime Martinez, B.S.AS.E

THESIS

Presented to the Faculty of the Graduate School of
The University of Texas at Austin
in Partial Fulfillment
of the Requirements
for the Degree of

MASTER OF SCIENCE IN ENGINEERING

THE UNIVERSITY OF TEXAS AT AUSTIN
August 2012

Dedicada a mis padres y a mi abuelito

Acknowledgments

I wish to thank my parents and my sister for their unconditional support. Besides being my only family in this country, they are and have been my sole support system in achieving my goals. The two hardest working individuals I know are my parents, and without their sweat and tears I would not have come this far. I would like to thank my advisor, Professor Venkat Raman, for giving me the opportunity to work on this project and introducing me to the world of CFD. For his guidance not only on my research, but also in life matters.

I would also like to thank Professor Armand Chaput for his immense support and help when I needed it the most. For genuinely caring about his students and inculcating my interest in aeronautics. Lastly, I would like to thank Professor Cesar Ocampo for his advice and words of encouragement.

Large Eddy Simulation Analysis of Non-Reacting Sprays Inside a High-G Combustor

Jaime Martinez, M.S.E.
The University of Texas at Austin, 2012

Supervisor: Venkatramanan Raman

Inter-turbine burners are useful devices for increasing engine power. To reduce the size of these combustion devices, ultra-compact combustor (UCC) concepts are necessary. One such UCC concept is the centrifugal-force based high-g combustor design. Here, a model ultra-compact combustor (UCC) with fuel spray injection is simulated using large eddy simulation (LES) and Reynolds-Averaged Navier-Stokes (RANS) methodologies to understand mixing and spray dispersion inside centrifugal-based combustion systems. Both non-evaporating and evaporating droplet simulations were carried, as well as the tracking of a passive scalar, to explore this multiphase system. Simulation results show that mixing of fuel and oxidizer is based on a jet-in-crossflow system, with the fuel jet issuing into a circulating oxidizer flow stream. It is seen that a a high velocity vortex-like ring develops in the inner core of the combustor, which has enough momentum to obstruct the path of combustion products. There is minimal fuel droplet and vapor segregation inside the combustor and enhanced turbulent mixing is seen at mid-radius.

Table of Contents

List of Tables

List of Figures

Chapter 1

Introduction

Inter-turbine burners (ITBs) are emerging as an useful concept for increasing aircraft engine power. In such systems, a combustor is added between the high and low pressure turbine stages, thereby providing additional energy that can be used for thrust or extracted as power. ITBs are the response to the ever increasing demand for reduced fuel burn, engine weight, and exhaust emissions, while maintaining the durability of an aircraft engine [31, 33]. Similar to the main combustor, ITBs should have minimal length in order to reduce weight. Since the ITB exhaust flows over the turbine blades, incomplete combustion products could detrimentally affect the lifecycle performance of turbine components through secondary reactions [2, 5, 6, 15, 31]. Ultra-compact combustors (UCC) are one technology which can be used for ITB applications [5, 6]. In UCCs, turning vanes are integrated into the combustor and the primary combustion zone is in a cavity protected from this core flow [31]. This design feature reduces the size of the system.

One type of UCC that has received considerable attention is the high-g combustor (HGC) design [3, 27, 32]. Fig. 1.1 illustrates a comparison of the UCC versus the traditional combustor configuration inside a typical gas turbine jet engine. Since the oxidizer flow is circular instead of longitudinal, a 66% length reduction is achieved when compared to conventional combustion systems with a diffuser and turbine inlet guide vanes [33]. Fig. 1.2 shows pictures of the experimental HGC both assembled (Fig. 1.2a) and opened (Fig. 1.2b), while Fig. 1.3 shows the modelled versions.

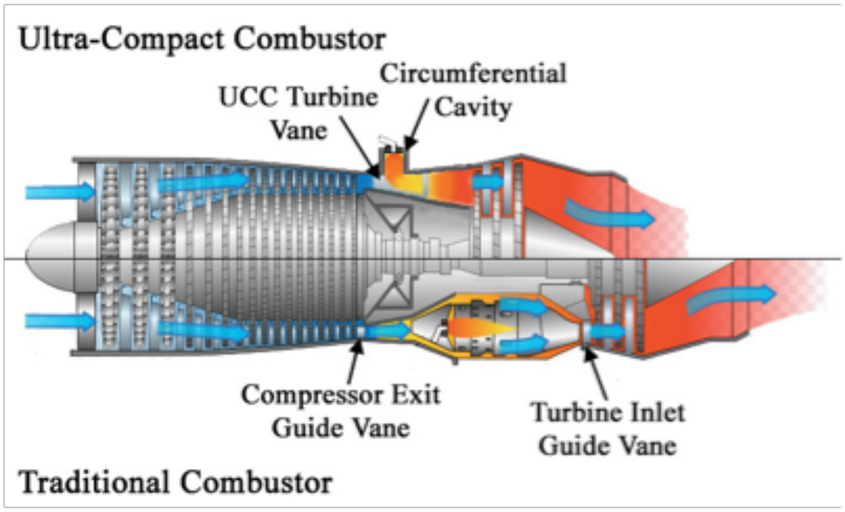

Figure 1.1: Traditional combustor (below), Ultra-Compact Combustor (above) [4].

The fuel and air swirl and react in the azimuthal direction of main cavity (see Figs. 1.2b and 1.3), where combustion takes place. Air is compressed in the outer plenum and travels through 6 sets of 8, 45°, angled passages that become the air inlets of the main cavity (see Fig. 1.3). The fuel is injected at a normal vector towards the centerline through 6 equidistant sprays located in between the sets of angled air inlets. This becomes a jet-in-crossflow system, where the fuel is injected into a stream of circulating oxidizer flow. The air inlets provide the swirling motion and centrifugal force that promotes burned

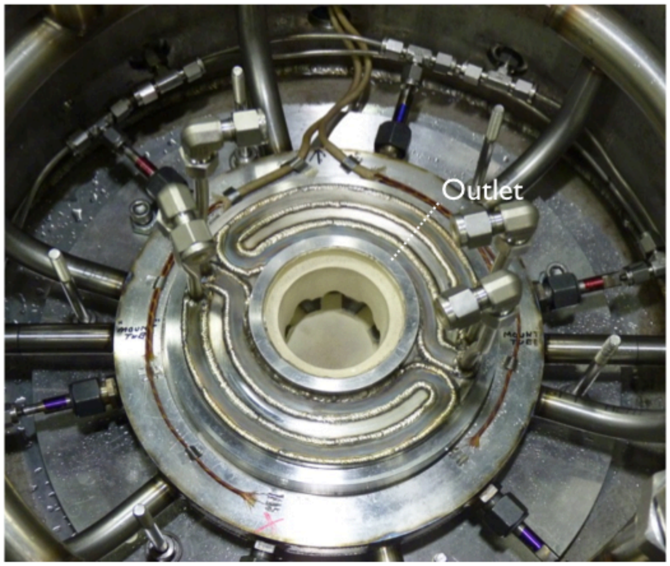

(a) Assembled system

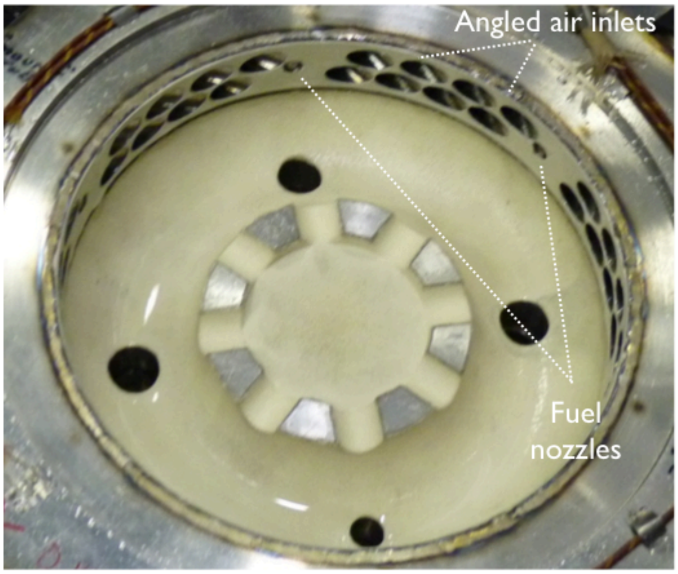

(b) Main cavity (bottom)

Figure 1.2: Experimental high-g combustor.

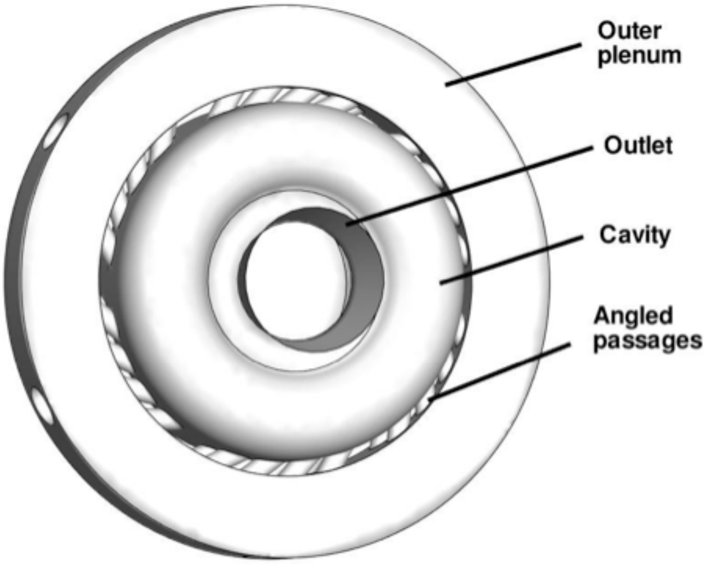

(a) Assembled system

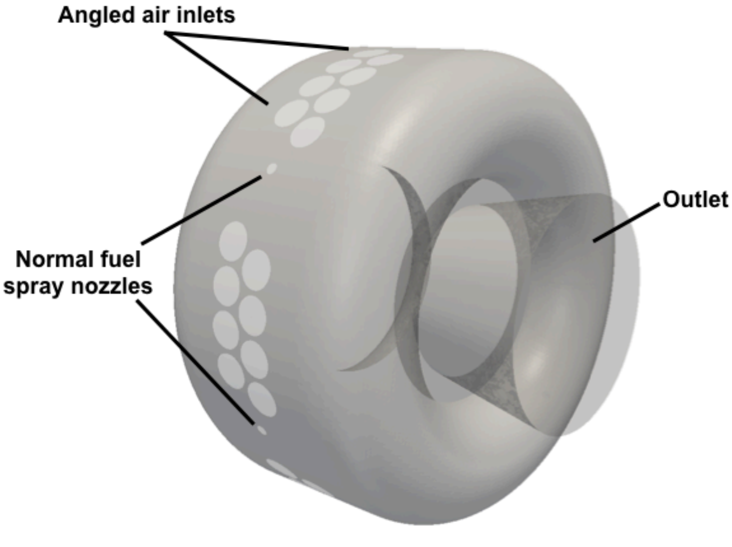

(b) Main cavity (isometric view)

Figure 1.3: Modelled high-g combustor.

mixture transport radially inward toward the centerline. The high velocity and direction of the gases in the cavity result in high centrifugal forces (e. g. order of 1000 g) which enhance reaction rates [33]. The centrifugal forces improve the transport of reactants and exhaust products as a result of buoyancy effects [7, 8]. They maintain the denser products (unburned gases) in the outermost radius, while the less dense (burned gases) travel radially inward towards the outlet. The centrifugal force or g-loading inside the UCC is simply calculated from,

$$g_{\,loading} = \frac{{U_T}^2}{g_c\, r}, \tag{1.1}$$

where U_T is the average tangential velocity inside the combustor, g_c is standard gravity, and r is the UCC's inner cavity radius.

The main concept of using high-g loading in combustion came from experiments from Lewis in the 1970's [8]. He wanted to achieve flame speeds greater than that of a turbulent flame and started investigating the effect of centrifugal forces on flame spreading in propane-air mixtures. In his experiments, he reached g-loadings of up to 10^4 g and observed a flame speed increase of up to 4 times that of a conventional turbulent flame without having to increase the flame inlet velocity [8]. He concluded that the burning rate of fuel-air mixture is proportional to the square root of the g-loading, and combustion in a centrifugal field greatly increases the buoyant forces that promote the mixing of combustion products [7]. Lewis attributed the increased flame speed to "bubbles" or eddies that move ahead of the flame front due to the centripetal acceleration. He noted that at loadings greater than 200 g, the increased bubble velocity dictated flame propagation, which created a faster and more turbulent flame [8]. This is important because a higher flame speed means that more fuel can be burnt in a smaller volume, which is the main goal of turbulent combustion. Zelina etal. [33] conducted experiments on a UCC based on some of Lewis' results and concluded that spray atomization is also a strong driver for the system performance. Here, it was noticed noticed that combustion efficiency is very sensitive to spray droplet size and liquid evaporation rates [33].

With this background, the primary focus of this research is to understand the turbulent flow inside a model UCC, in order to better describe the mixing and combustion processes. In order to model the fuel spray injection inside the UCC, a Eulerian-Lagrangian modeling approach is taken. This means that the UCC's gaseous flow field is modeled using the Eulerian-based NS equations, while the liquid-fuel spray is modeled in a Lagrangian-based fashion. This creates a velocity coupling, which is taken into account with spray source terms in the gaseous NS equations and in the Lagrangian droplets' relative velocities. This thesis only focuses on fuel mixing and the spray-based dispersion of fuel inside the UCC, so there are no chemical reactions nor combustion modeling. However, a fuel mixture fraction transport equation is solved to analyze gaseous fuel dispersion. Various simulations were conducted with both LES and RANS numerical methods to analyze spray injection and fuel mixture fraction. Focus is given to spray injection, so simulations with varying mesh size and droplet diameter were carried out as well to analyze solution quality and effects of buoyancy forces. This thesis is organized into 4 major parts: Modeling turbulent gas phase flow inside UCC, spray injection modeling, simulation of the UCC, and results and discussion.

Chapter 2

Modeling Turbulent Gas Phase Flow Inside UCC

The majority of the flows in real world applications are turbulent. The flow inside a UCC is necessarily turbulent due to the high Reynolds number. The motivation to study turbulent flow in combustion relies on its ability to mix and transport fluids better and at a higher rate than laminar flow. Combustion greatly benefits from the turbulent flow, through enhanced fuel/air mixing leading to rapid energy release. Turbulent flow enhances the mixing of reactants and rate of momentum and heat transfer, which are essential to efficient combustion [24].

Turbulent flow is characterized by its random nature, but random in the context that turbulence is neither certain nor impossible [24]. Any laminar flow is fully described by the Navier-Stokes (NS) equations, where the velocity field is a certain quantity. However, direct solution of the NS equations is not feasible due to the large computational requirement associated with resolving the range of length and time scales. An alternative approach is to seek only the statistics of the velocity and combustion-related fields. In this sense, the turbulent flow is treated as random fields, and a statistical approach is devised to evolve the one-point one-time statistics of the required quantities. These statistics revolve around the probability density function (PDF), which is an essential tool that quantifies random variables. Statistics come into play both in the simulation models and most importantly when validating a solution to the modeled NS equations. When numerically simulating turbulent flows the most widely used techniques are Reynolds-averaged Navier-Stokes (RANS) and large-eddy simulation (LES). The UCC's gaseous flow field is modeled using both of these numerical techniques. This chapter deals with the gaseous Eulerian part of the modeling, while Chapter 3 deals with the Lagrangian spray modeling. This chapter also gives a brief introduction to the turbulence energy cascade theory, explains how OpenFOAM implements the RANS and LES methods for numerically solving the NS equations with spray source terms, and describes the transport equation for mixture fraction.

2.1 Energy Cascade and Kolmogorov Scales

One of the most important concepts in understanding the behavior of turbulence is the energy cascade theory. It states that large turbulent scales contain kinetic energy, which gets transferred inviscidly to progressively smaller scales until the local Reynolds number is low enough to allow viscosity to dissipate the energy [24]. During turbulent combustion, mixing is initiated by the large scales where convection generates high velocity gradients in the flow. But it is up to the energy dissipating small-scales to finalize the mixing process so that the fuel and air are molecularly mixed, which is a precursor for chemical reactions. Therefore, it is very important to understand the behavior of turbulent length scales and the rate at which turbulent kinetic energy is being transferred from large to small scales.

Kolmogorov explained the turbulent scale phenomena even further through a series of hypotheses [24], which deduced powerful properties that facilitated the statistical description of turbulent flows. The first hypothesis stated that at high Reynolds numbers small scale eddies are locally isotropic because due to the chaotic nature of the anisotropic large eddies, their directional bias is lost with the energy cascade. The threshold between large and small scales is marked by the length scale that contains the smallest energy, ℓ_{EI}, which can be approximated as one sixth of the largest eddy size, ℓ_o.

Kolmogorov argued that the geometry of the large eddies was lost as well with the energy cascade, so the statistics of the small scales must be universal and described by the kinematic viscosity ν and the energy dissipation rate ϵ. This was his second hypothesis, which identified the smallest turbulent scales (later referred to commonly as the Kolmogorov length scale) inside a universal equilibrium range ($< \ell_{EI}$). His third hypothesis splits the equilibrium range into the inertial subrange and the dissipation range. In the inertial subrange only inertial forces transfer the energy form the large scales to the Kolmogorov's scales, so it acts as a transition zone. In the dissipation range, viscous forces dominate and dissipate the energy at the smallest scale level [24]. Fig. 2.1 illustrates Kolmogorov's lengthscales and what simulation types are used to explicitly resolve them.

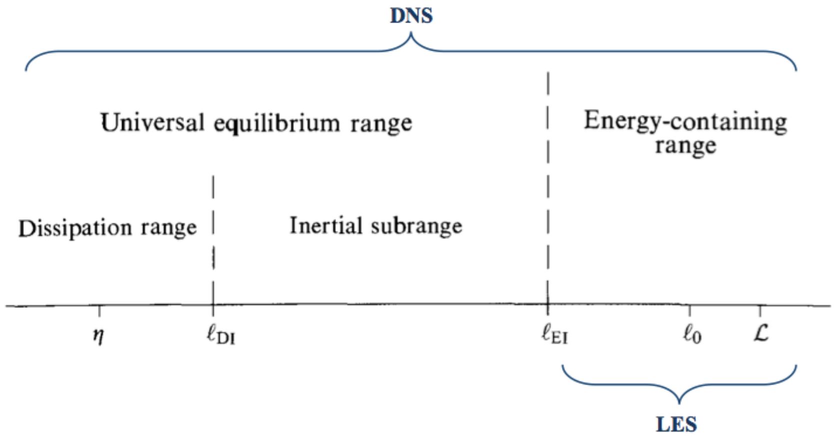

Figure 2.1: Turbulent lengthscales and ranges on a logarithmic scale at high Reynolds number [24].

2.2 RANS

RANS is the most widely used method for solving fluid motion today. It is so widely used because it is very computationally inexpensive, while giving an averaged solution of the flow field. The governing equations for a multiphase-flow that describe both the continuous gas phase and the motion of spray droplets are the NS equations with a spray momentum source term [28]. RANS consists of time averaging the NS equations, modeling the Reynolds stress tensor that arises from the time average, and solving for the averaged velocity field. The velocity $\langle U(\mathbf{x},t)\rangle$ is decomposed into the mean velocity $\overline{\mathbf{u}}(\mathbf{x},t)$ plus a fluctuating component $u'(\mathbf{x},t)$ as shown below,

$$\langle U(\mathbf{x},t)\rangle = \overline{\mathbf{u}}(\mathbf{x},t) + u'(\mathbf{x},t). \tag{2.1}$$

The averaged incompressible continuity and momentum NS equations for the continuous gas phase are [1]:

$$\frac{\partial \overline{\rho}}{\partial t} + \nabla \cdot (\overline{\rho}\overline{\mathbf{u}}) = \dot{\rho}^s \tag{2.2}$$

and

$$\frac{\partial (\overline{\rho}\overline{\mathbf{u}})}{\partial t} + \nabla \cdot (\overline{\rho}\overline{\mathbf{u}}\overline{\mathbf{u}}) + \nabla \overline{p} - \nabla \cdot \tau_{ij} - \overline{\rho}\mathbf{g} + \mathbf{F}^s = 0, \tag{2.3}$$

where $\overline{\rho}$ is the averaged gas phase air density, $\dot{\rho}^s$ is the evaporation rate (derived in 3.3.1), $\overline{p}$ is the mean pressure, $\mathbf{g}$ is the vector acceleration due to gravity, and $\mathbf{F}^s$ is the momentum gain per unit volume source term due to the spray (derived in 3.1) [1]. The averaged density $\overline{\rho}$ is solved through the continuity equation (2.2) and the averaged velocity $\overline{\mathbf{u}}$ through the momentum equation (2.3). τ_{ij} is the viscous stress tensor and is equal to:

$$\tau_{ij} = \mu \left(\frac{\partial \overline{u}_i}{\partial x_j} + \frac{\partial \overline{u}_j}{\partial x_i} \right) - \overline{\rho}\,\overline{u_i' u_j'}. \tag{2.4}$$

μ is the gas phase dynamic viscosity and $-\overline{\rho}\,\overline{u_i' u_j'}$ is the Reynolds stress tensor that is modeled to bring closure to the NS equations. From the turbulent-viscosity hypothesis, which states that the deviatoric Reynolds stress is proportional to the mean rate of strain [24], the Reynolds stress is given by

$$-\overline{\rho}\,\overline{u_i' u_j'} = \mu_T \left(\frac{\partial \overline{u}_i}{\partial x_j} + \frac{\partial \overline{u}_j}{\partial x_i} \right) - \frac{2}{3}\overline{\rho}\mathbf{k}\delta_{ij}, \tag{2.5}$$

where $\mathbf{k}$ is the turbulent kinetic energy and μ_T is the turbulent viscosity (or eddy viscosity).

Using equation (2.5), equation (2.3) can be rewritten as

$$\frac{\partial (\overline{\rho}\overline{\mathbf{u}})}{\partial t} + \nabla \cdot (\overline{\rho}\overline{\mathbf{u}}\overline{\mathbf{u}}) + \nabla \left(\overline{p} + \frac{2}{3}\rho\mathbf{k} \right) - \nabla \cdot \left[\mu_{eff} \left(\nabla\overline{\mathbf{u}} + (\nabla\overline{\mathbf{u}})^T \right) \right] - \overline{\rho}\mathbf{g} + \mathbf{F}^s = 0, \tag{2.6}$$

where

$$\mu_{eff}(\mathbf{x}, t) = \mu + \mu_T(\mathbf{x}, t) \tag{2.7}$$

is the effective viscosity and μ the gas phase kinematic viscosity. Full closure is obtained by modeling the time dependent turbulent viscosity μ_T through the compressible flow version of the k-ϵ turbulence model. In this two equation model the turbulent viscosity is modeled as

$$\mu_T = \frac{\overline{\rho} C_\mu \mathbf{k}^2}{\epsilon}, \tag{2.8}$$

where $\mathbf{k}$ is the turbulent kinetic energy, ϵ is the turbulent dissipation rate, and $C_\mu = 0.09$. The transport equations for $\mathbf{k}$ and ϵ [17] are

$$\frac{\partial\left(\overline{\rho}\mathbf{k}\right)}{\partial t} + \frac{\partial}{\partial x_j}\left(\overline{\rho}\mathbf{k}\overline{u}_j\right) = \frac{\partial}{\partial x_j}\left[\left(\mu + \frac{\mu_T}{\sigma_k}\right)\frac{\partial \mathbf{k}}{\partial x_j}\right] + G - \overline{\rho}\epsilon \tag{2.9}$$

and

$$\frac{\partial\left(\overline{\rho}\epsilon\right)}{\partial t} + \frac{\partial}{\partial x_j}\left(\overline{\rho}\epsilon\overline{u}_j\right) = \frac{\partial}{\partial x_j}\left[\left(\mu + \frac{\mu_T}{\sigma_\epsilon}\right)\frac{\partial \epsilon}{\partial x_j}\right] + \frac{\epsilon}{\mathbf{k}}\left(C_1 G - C_2\overline{\rho}\epsilon\right), \tag{2.10}$$

with the constants:

$$C_1 = 1.44 \qquad C_2 = 1.92 \qquad \sigma_K = 1.0 \qquad \sigma_\epsilon = 1.3. \tag{2.11}$$

In equations (2.9) and (2.10) G represents the generation of turbulent kinetic energy due to mean velocity gradients. It is defined as

$$G = \mu_T S^2, \tag{2.12}$$

where S is the modulus of the mean strain rate tensor $\overline{\mathbf{S}}_{ij}$,

$$S = \sqrt{2\overline{\mathbf{S}}_{ij}\overline{\mathbf{S}}_{ij}}, \tag{2.13}$$

with $\overline{\mathbf{S}}_{ij}$ equal to,

$$\overline{\mathbf{S}}_{ij} = \frac{1}{2}\left(\frac{\partial \overline{u}_i}{\partial x_j} + \frac{\partial \overline{u}_j}{\partial x_i}\right). \tag{2.14}$$

OpenFOAM does not take into account the droplet-turbulence interaction because a spray source term does not appear in the previous turbulence equations. The turbulence modulation due to the presence of a spray is a complex process that is not yet fully understood. Turbulence generation due to spray droplets is vastly influenced by how diluted the spray is, ratio of particle size to characteristic turbulent length scale, and velocity difference between the discrete and gaseous phases [16]. Some attempts of turbulence modulation consist of adding a sink spray source term in the $k-\epsilon$ equations, which reduces turbulent energy in the presence of a liquid parcel. However, this assumes that liquid volume fraction is negligible and that the droplets are small in comparison to the turbulent length scales [1]. Due to the lack of a well-established method of introducing spray turbulence modulation, OpenFOAM's standard $k-\epsilon$ model without a spray source term is used. Therefore, turbulence is only influenced indirectly by the momentum transfer and generation of velocity gradients from the Lagrangian phase [22].

2.3 LES

Unlike RANS, LES is based on the concept of filtering, where the most energetic scales are directly solved while the effect of small scales is modeled. It is a compromise between directly solving the NS equations (DNS) and RANS because LES explicitly resolves the scales that describe the majority of the flow domain. This translates into a much more detailed representation of the flow and its major structures. Another advantage of LES is that it is less computationally expensive than DNS because it avoids the cost of explicitly resolving the small-scale motions and the flow can be resolved on a coarser grid than DNS.

In LES, the velocity field $U(\mathbf{x}, t)$ is decomposed into the sum of a filtered component $\widetilde{\mathbf{u}}(\mathbf{x}, t)$ and a residual or sub-grid scale (SGS) component $u'(\mathbf{x}, t)$ as shown below,

$$U(\mathbf{x}, t) = \widetilde{\mathbf{u}}(\mathbf{x}, t) + u'(\mathbf{x}, t). \tag{2.15}$$

The filtered component represents the resolved velocity of the large-scale motions or large eddies. The most common filter functions are the box filter, the Gaussian filter, and the sharp spectral filter [24]. Each filter function uses a specified filter width Δ. In practical computations, the filter width is implicitly set by the computational mesh. In this sense, the filtering function does not enter the calculations. The local filter width is obtained based on the computational cell volume, which marks the threshold of the large-scale motions. Therefore, Δ should be at most comparable to l_{EI} in order to accurately resolve large-scales [24]. In compressible flows, a Favre-filtered field is most commonly used in order to account for the density changes. For a space and time dependent variable, $\widetilde{Q}(\mathbf{x}, t)$, the Favre-filtered [24] field can be written as

$$\widetilde{Q}(\mathbf{x}, t) = \frac{1}{\overline{\rho}} \int_{-\infty}^{+\infty} \rho(\mathbf{y}, t) Q(\mathbf{y}, t) G\left(\mathbf{y} - \mathbf{x}\right) d\mathbf{y}, \tag{2.16}$$

where $\overline{\rho}$ is the filtered density, and G is the filtering kernel that typically operates over a finite domain. By filtering the Navier Stokes equations, the effect of large energy-containing scales is retained, while the effect of smaller sub-filter scales needs to be modeled. LES captures the large-scale mixing accurately, which is deemed sufficient for capturing flames far from extinction.

Applying the filtering operation to the continuity and momentum equations leads to the following filtered transport equations, which are similar to their RANS counterparts.

$$\frac{\partial \overline{\rho}}{\partial t} + \nabla \cdot \left(\overline{\rho}\widetilde{\mathbf{u}}\right) = \dot{\rho}^s, \tag{2.17}$$

and

$$\frac{\partial \overline{\rho}\widetilde{\mathbf{u}}}{\partial t} + \nabla \cdot \left(\overline{\rho}\widetilde{\mathbf{u}}\widetilde{\mathbf{u}} + \overline{p}\delta - \widetilde{\tau}\right) + \nabla \cdot \mathcal{M}^u + \mathbf{F}^s = 0, \tag{2.18}$$

where $\widetilde{\mathbf{u}}$ is the filtered velocity field, $\overline{p}$ is the filtered pressure, and τ is the viscous stress tensor. $\widetilde{(\cdot)}$ represents a filtered LES field.

$$\widetilde{\tau} = \widetilde{\mu}\left(2\widetilde{\mathbf{S}}\right) - \frac{2}{3}\widetilde{\mu}\left(\nabla \cdot \widetilde{\mathbf{u}}\right)\delta, \tag{2.19}$$

where $\widetilde{\mu}$ is the filtered dynamic (shear) viscosity and $\widetilde{\mathbf{S}}$ is the filtered strain rate tensor.

$$\widetilde{\mathbf{S}} = \frac{1}{2}\left(\nabla\widetilde{\mathbf{u}} + (\nabla\widetilde{\mathbf{u}})^T\right). \tag{2.20}$$

In equation (2.18), $\mathcal{M}^u$ is the SGS stress that arises from the filtering of the nonlinear convection term and requires modeling. In this study, a Smagorinsky-type eddy-viscosity model is used for closure.

$$\mathcal{M}^u = \overline{\rho}\left(\widetilde{\mathbf{u}\mathbf{u}} - \widetilde{\mathbf{u}}\widetilde{\mathbf{u}}\right) = 2\mu_t\left(\widetilde{\mathbf{S}} - \frac{1}{3}\left(\nabla \cdot \widetilde{\mathbf{u}}\right)\delta\right) \tag{2.21}$$

where turbulent viscosity $\mu_t = C_s \overline{\rho} \Delta^2 |\widetilde{\mathbf{S}}|$. An algebraic model is used for dynamically determining the value of modeling constant C_s [9]. Note that just like in the RANS equations, the sub filter models are left unchanged for the case with spray droplets, which is a strong assumption. In general, the presence of sprays will alter the small scale dissipation, but this aspect is almost always neglected in LES computations.

2.3.1 Mixture Fraction

A conserved scalar is used to analyze the fuel dispersion inside the UCC. This is done by introducing fuel into the combustor in a gaseous state through all the fuel inlets, where density changes are neglected and the flow is assumed to be incompressible due to the low injected velocities. The gaseous flow field is represented by the momentum NS equations mentioned before, but in order to provide a measure of fuel dispersion inside the combustor, fuel mixture fraction is used, Z. It is modeled as a conserved scalar,

$$Z = \frac{X_i - X_{i,OX}}{X_{i,fuel} - X_{i,OX}}, \tag{2.22}$$

where X_i is the elemental mass fraction for element i and the subscripts OX and $fuel$ denote the values at the oxidizer and fuel stream inlets respectively. Z is carried through the flow by solving its transport equation,

$$\frac{\partial Z}{\partial t} + \nabla \cdot (\mathbf{u} Z) - \nabla \cdot \nu_{eff} \nabla Z = 0, \tag{2.23}$$

where ν_{eff} is the effective viscosity, which is the sum of the laminar viscosity and the turbulent viscosity obtained from either equations (2.8) or (2.21) depending on RANS or LES modeling. The transport velocity $\mathbf{u}$ is either the averaged velocity, $\overline{\mathbf{u}}$, or Favre-filtered velocity, $\widetilde{\mathbf{u}}$, depending on the type of simulation.

Chapter 3

Spray Injection Modeling

In the UCC as well as all aircraft engines, the liquid fuel is injected into the combustion chamber in the form of a finely atomized spray. This spray is an example of a two-phase flow, which consists of a continuous and a discrete phase. A spray is commonly generated through atomization and a series of break-up stages; the continuous liquid phase is broken down from ligaments to droplets through atomization and the droplets are further broken down through collisions and aerodynamic forces as shown in Figure 3.1. After the droplet generation and break-up, evaporation occurs, leading to gas phase fuel that is then transported by turbulent convection [26].

Modeling a spray system is a complex task due to the coupled fluid-dynamics and transport phenomena that occur among the droplets, and with the carrying gas. The overall exchange of mass, momentum, and energy of the system can not be determined without some detailed knowledge at a fine scale, which creates a scale coupling reminiscent of the turbulent energy cascade theory. The modeling is further complicated with the introduction of turbulent combustion since the evaporation rate strengthens the coupling between the discrete and gaseous phases and imposes a limit on the droplets'

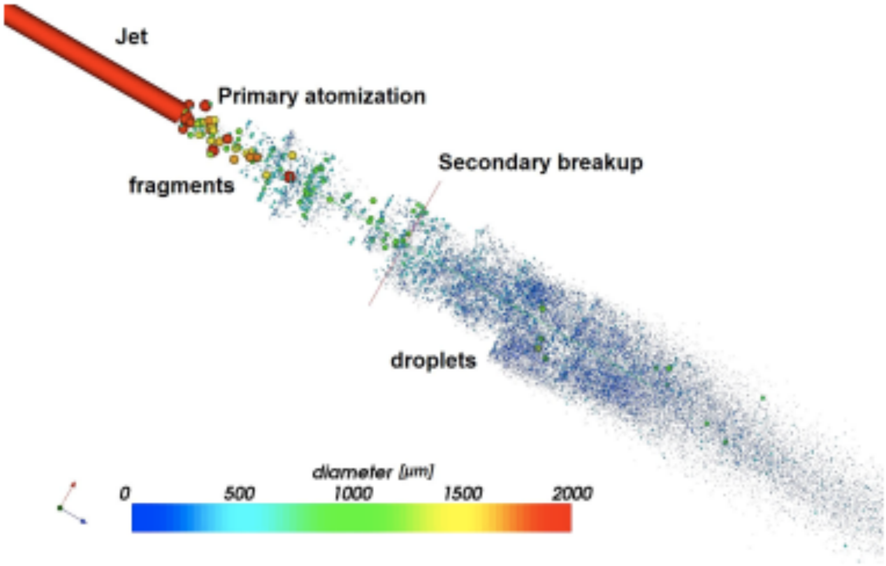

Figure 3.1: Illustration of the droplet break-up phases in a spray colored by droplet diameter [10].

lifetime [26]. The droplets' interaction with another surrounding gas (oxidizer in non-premixed combustion) adds more complexity to the system. Fuel mixing, chemical and turbulent time scales, and ignition time become critical components in determining the fuel burning rate and overall combustion efficiency.

The approach used in this work consists of three steps. The atomization part is not modeled, and the result of atomization is considered as spray droplets of known distribution entering the domain. First, the dispersed liquid droplets are considered as non-evaporating particles that are only interacting with the carrying gas. The continuous gas phase is solved in the

Eulerian framework and the liquid spray is treated by a standard discrete droplet method (DDM) [21]. In order to increase computational efficiency, a collection of particles with constant properties are treated as parcels. Each parcel represents a class of identical, non-interacting droplets, that are tracked in physical space in a Lagrangian manner as they interact with the continuous gas phase flow [21]. Second, once the droplets reach a steady state with the surrounding turbulent flow, evaporation is considered. The start of evaporation is defined by a fixed saturation level of fuel mass fraction that depends on the surrounding gas' temperature and pressure. A mixture fraction scalar is then used to describe the mixing between the gaseous fuel and oxidizer. Finally, an ignition time and location is specified inside the combustion chamber, where gaseous fuel and oxidizer are instantaneously converted into burned gases and flame propagation begins [25].

3.1 Lagrangian Approach For Droplets

The droplets' properties are solved in the Lagrangian space and their effect on the continuous gas flow is taken into account through the spray's evaporation and momentum source terms ($\dot{\rho}^s$ and $\mathbf{F}^s$ in the NS continuity and momentum equations (2.2), (2.3), (2.17), and (2.18)). The momentum source term $\mathbf{F}^s$ is calculated at every droplet time step in the Lagrangian frame, summed over all of the droplets, and added into the NS momentum equation at each Eulerian time step to update the flow velocity. The momentum source

$\mathbf{F}^s$ is calculated as

$$\mathbf{F}^s = \sum_N f_d, \tag{3.1}$$

where N is the number of droplets in the system and f_d is the droplet momentum contribution on a unit volume of fluid ΔV, which is equal to the difference in droplet momentum between the time it enters (t_{in}) and leaves (t_{out}) a computational cell,

$$f_d = \frac{m_d}{\Delta V} \frac{(\mathbf{u}_d)_{t_{out}} - (\mathbf{u}_d)_{t_{in}}}{t_{out} - t_{in}}. \tag{3.2}$$

In equation (3.2), $\mathbf{u}_d$ corresponds to the droplet's local velocity and m_d is the droplet's mass, which is (based on the assumption of a spherical droplet)

$$m_d = \frac{1}{6}\rho_d \pi D_d^3, \tag{3.3}$$

where ρ_d is a droplet's liquid density and D_d its diameter. In order to calculate $\mathbf{u}_d$ and a droplet's local position x_d, a simple force balance on a single droplet is performed,

$$m_d \frac{d\mathbf{u}_d}{dt} = \mathbf{F}_d + \mathbf{F}_g, \tag{3.4}$$

where only drag, $\mathbf{F}_d$, and gravity, $\mathbf{F}_g$, forces are considered. When including expressions for these, equation (3.4) becomes

$$\frac{d\mathbf{u}_d}{dt} = -\frac{\mathbf{u}_d - \mathbf{u}}{\tau_u} + \mathbf{g}, \tag{3.5}$$

where $\mathbf{u}$ is either the RANS or LES Eulerian gas phase velocity and τ_u is the momentum relaxation time,

$$\tau_u = \frac{8m_d}{\pi\rho C_d D_d^2|\mathbf{u}_d - \mathbf{u}|} = \frac{4}{3}\frac{D_d\rho_d}{\rho C_d|\mathbf{u} - \mathbf{u}_d|}. \tag{3.6}$$

The drag coefficient C_d is based on the droplets' Reynolds number Re_d, which is defined as,

$$C_d = \begin{cases} \frac{24}{Re_d}\left(1 + \frac{1}{6}Re_d^{2/3}\right) & Re_d < 1000 \\ 0.424 & Re_d \geq 1000 \end{cases} \tag{3.7}$$

where

$$Re_d = \frac{\rho|\mathbf{u} - \mathbf{u}_d|D_d}{\mu}, \tag{3.8}$$

and ρ and μ are the gas' density and dynamic viscosity respectively.

3.2 Particle Dispersion

Understanding the interaction between droplets and the carrying fluid is the basis of being able to model a spray system. Droplet dispersion stems from the flow interaction between the carrying gas and its surroundings. Stokes number, St, is the main dimensionless parameter used to describe droplet dispersion and it shows how accurate droplets capture the flow characteristics of the carrying fluid [25]. It is the ratio of the droplet to carrier fluid time scales. When applying it to turbulent sprays, the definition used for the UCC is,

$$St = \frac{\tau_p}{\tau_k}, \tag{3.9}$$

where τ_p is the characteristic droplet relaxation delay:

$$\tau_p = \frac{\rho_l D_d^2}{18\mu}, \tag{3.10}$$

and τ_k is the gas phase Kolmogorov timescale:

$$\tau_\kappa = \left(\frac{\nu}{\epsilon}\right)^{1/2}. \tag{3.11}$$

Combining these yields the Stokes number equation,

$$St = \frac{\rho_l {D_d}^2}{18\mu} \left(\frac{\nu}{\epsilon}\right)^{-1/2}, \tag{3.12}$$

where ρ_l is the liquid's density, D_d is the droplet's diameter, ν and μ are the carrying gas' kinematic and dynamic viscosities respectively, and ϵ is the turbulent energy dissipation rate [29]. The energy dissipation ϵ is estimated through the formula,

$$\epsilon = {C_\mu}^{0.75} \frac{k^{1.5}}{l}, \tag{3.13}$$

where l is the turbulent characteristic length scale, taken as 50 % of the angled air inlets width, and k is the turbulent kinetic energy estimated with the following equation for isotropic turbulence,

$$k = \frac{3}{2} \left(U_a I\right)^2, \tag{3.14}$$

where U_a is the angled air inlet velocity magnitude and I is a turbulent intensity of 5 %. If $St \ll 1$, the droplet response time is much shorter than the fluid's, so small perturbations in the flow can be captured at a greater detail by the droplets. If $St \gg 1$, then a time lag exists between the fluid's motion and the droplets to the point where the droplets do not respond fast enough to flow perturbations.

When analyzing the flow of non-evaporating droplets, varying the Stokes number provides insight into how droplet size and inertia affect the droplets' dispersion and mixing. This is important because fuel droplet mixing affect fuel concentration and evaporation rates, which alter combustion . DNS simulations by Reveillon and Demoulin (2006) have shown interesting droplet behavior in non-reacting turbulent flows, droplet evaporation, and combustion when varying Stokes number. Their results show that for $St = 0.17$ the droplets segregate in weak vorticity areas because they do not possess enough inertia to reside in vortex cores, which diminishes dispersion. For high Stokes numbers, 5.6, a much more dispersed spray occurs because there is enough inertia for the droplets to cross high vorticity areas, which results in better droplet mixing. The most interesting case happens for a Stokes number close to unity. Here, maximum droplet segregation occurs, which means that clusters with high liquid droplet density are scattered throughout the domain [25]. This thesis explores this interesting regime in the UCC, where the Stokes number is close to unity.

3.2.1 Droplet size distribution

This thesis explores the effects of both constant and variable droplet size distributions in spray impingement. Since atomization is not being considered, the part where the majority of the droplet breakup occurs, imposing a PDF at the spray inlet to include some of the effects of the varying droplet sizes is appropriate. The chosen PDF is the Rosin Rammler particle size distribution because it is well established and the most commonly used particle size PDF in spray modeling. It is based on the droplet's diameter $\mathbf{D_d}$ and returns a droplet diameter distribution by specifying a mean diameter, D_d^m, and a particle size range, n, as shown below,

$$F_M(\mathbf{D_d}) = 1 - exp\left(-\left(\frac{\mathbf{D_d}}{D_d^m}\right)^n\right). \tag{3.15}$$

3.3 Evaporation

After the droplets have reached equilibrium with the surrounding turbulent flow and a set boiling pressure, evaporation starts. The process is governed by the droplet evaporation rate, which reduces the size of the droplet until its liquid mass is converted into the gaseous phase. Droplet dispersion and evaporation play a major role in combustion because depending on how the droplets disperse, once they evaporate clusters of high fuel concentration can generate, which decrease combustion efficiency. Results by Reveillon and Demoulin (2006) show that this happens when St is close to unity and the droplets show maximum segregation. As evaporation starts, the surrounding vapor in these clusters gets closer to its saturation level, which starts reducing the vapor flux from the droplets' surface and the overall evaporation rate. This evaporation scenario is summarized by Fig. 3.2.

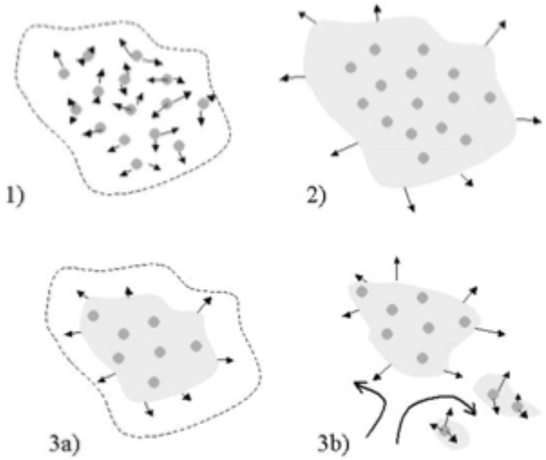

Figure 3.2: Three-step evaporation process [25].

(1) Droplets start evaporating normally at a fast rate. (2) As the vapor from the initially evaporated droplets starts reaching its saturation level in clusters of high droplet density, the evaporation rate dramatically decreases. (3) The remaining droplets inside these clusters are evaporated only if (3a) diffusion and turbulent mixing reduce the vapor concentration in the cluster or (3b) turbulent motion gives droplets enough momentum to escape the cluster and into a lower vapor concentration [25]. Reveillon and Demoulin also noticed that for $St << 1$ droplets segregate in weak vorticity areas and are minimally dispersed. For $St >> 1$, the droplets have enough inertia to cross high vorticity areas and vast dispersion occurs.

3.3.1 Evaporation rate

In order order to calculate the total evaporation rate $\dot{\rho}^s$ in equations (2.2) and (2.17), a summation over all spray parcels in the cell volume is done [20],

$$\sum_V N_p \dot{m}_d = -\int_V \dot{\rho}^s dV = -V\dot{\rho}^s, \tag{3.16}$$

where V is the volume of the cell, $\dot{m}_d$ is a single droplet's evaporation rate, and N_p is the statistical number of droplets in a parcel. The evaporation rate dictates how fast a droplet gets converted into gas and its liquid mass becomes added gas in the system. In this study a standard evaporation model is followed, where droplet evaporation occurs when the fuel vapor pressure is lower than the combustion chamber's pressure [19]. The only mass transfer occurs from the liquid to the gas phase; condensation is not considered.

A single droplet's evaporation rate is quantified as a rate of size reduction based on the droplet's diameter D_d, which is modeled as [20],

$$\dot{m}_d = -\frac{d}{dt}\left(\frac{\pi}{6}{D_d}^3\rho_v\right) = \pi D_d \rho_v Sh \mathfrak{D}\, ln(1+B), \tag{3.17}$$

where ρ_v is the density of the fuel vapor close to the droplet's surface (estimated using the ideal gas law), $\mathfrak{D}$ is the droplet's mass diffusion, B is Spalding's mass transfer number, and Sh is the Sherwood number defined as,

$$Sh = 2.0 + 0.6Re^{1/2}Sc^{1/3}, \tag{3.18}$$

where Sc is the droplet's Schmidt number.

From equation (3.17) the droplet's evaporation rate $\dot{m}_d$, based on D, is given by,

$$\dot{m}_d = -\frac{m_d}{\tau_e}, \quad \frac{dD_d}{dt} = -\frac{D_d}{3\tau_e}, \tag{3.19}$$

where the evaporation relaxation time τ_e is

$$\tau_e = \frac{m_d}{\pi D_d \rho_v Sh \mathfrak{D}\, ln(1+B)}, \tag{3.20}$$

with m_d being the droplet's mass.

Chapter 4

Simulation of UCC

All of the simulation work in this thesis was done using OpenFOAM (Open Field Operation And Manipulation) [18], an open source CFD object-oriented software toolkit with ability to simulate problems that range from molecular dynamics to finite element analysis. It was designed to facilitate research in physical modeling by taking a modular approach where the physics, numerics, and meshing parts of a problem are separated from each other [12]. Since OpenFOAM is a C++ based software, it takes advantage of its object-oriented framework. This gives the user an extensive ability to tailor OpenFOAM to fit his or her research needs by implementing new numerical solvers, discretization schemes, and complex geometries without modifying the entire source code. It also includes an extensive library of solvers that the user can modify to add new features, or reference when creating one from scratch. This modular approach allows for extensive code re-use, fewer bugs, and the user only needs to understand the main modules without going deep in the source code. This chapter explains the OpenFOAM numerical solvers used to simulate the flow inside the UCC and the simulations that were carried to explore spray droplet dispersion and fuel mixture fraction.

4.1 Numerical Implementation

OpenFOAM is defined in a UNIX environment and recognizes a problem through a case folder, where the problem's physics, numerics, boundary conditions, and mesh files are included. Each case folder is governed by the type of numerical solver the user chooses based on the problem's flow type and physics. These solvers use numerical discretization schemes to solve the RANS or LES NS equations. The two OpenFOAM solvers that were used to simulate spray injection and fuel mixture fraction inside the UCC were dieselFoam and an altered version of pisoFoam, respectively.

DieselFoam is a low-Mach number compressible flow solver created to simulate diesel spray injection in internal combustion engines from injection to combustion. Some of the features of dieselFoam include its ability to model a spray using a Eulerian-Lagrangian approach, atomization and evaporation modeling, use of various PDFs to describe droplet size, and simple chemistry and combustion modeling. Since only droplet dispersion and evaporation are analyzed in this work, the other features were not used. In OpenFOAM, all of the numerical schemes and matrix equation solvers used to discretize each term in the RANS and LES NS equations are defined in the `fvSchemes` and `fvSolution` files (see App. A). DieselFoam uses a PISO (Pressure Implicit Split Operator) algorithm to solve the equations for pressure and velocity. This is an iterative procedure used in transient solvers, which evaluatess a solution based on initial conditions and corrects it every time step. A second-order Euler implicit scheme is used for time advancement, while the convective and diffusive terms are discretized using second-order Gaussian integration with a linear interpolation scheme. Pressure and velocity equations are solved using preconditioned conjugate and bi-conjugate gradient solvers with tolerances of 1×10^{-6}.

In the mixture fraction case, the pisoFoam solver was modified to solve for the mixture fraction transport equation (2.23) in addition to the NS equations, the name of the new solver became mixFoam. The additional transport equation was implemented by adding the file `ZEqn.H` (see App. B.3) inside the pisoFoam source code. MixFoam also uses the PISO algorithm to solve for pressure and velocity. It is a standard incompressible flow solver that is used for transient simulations. Since density and spray source terms are not being solved for, mixFoam has a much shorter computational time than dieselFoam. The same numerical schemes and matrix equation solvers used for spray injection were used for mixture fraction (see App. B).

4.2 Simulation Conditions

A total of 7 simulations were carried out in this thesis to analyze spray droplet and gaseous fuel dispersion inside the UCC. The simulations are divided into two major parts: spray injection and mixture fraction. Fig. 4.1 shows all of the simulations that are presented in this work, along with simulation type and mesh used. The spray injection simulations are subdivided into constant and variable droplet diameter, which were solved using both LES and RANS methods. The constant droplet size simulations were performed

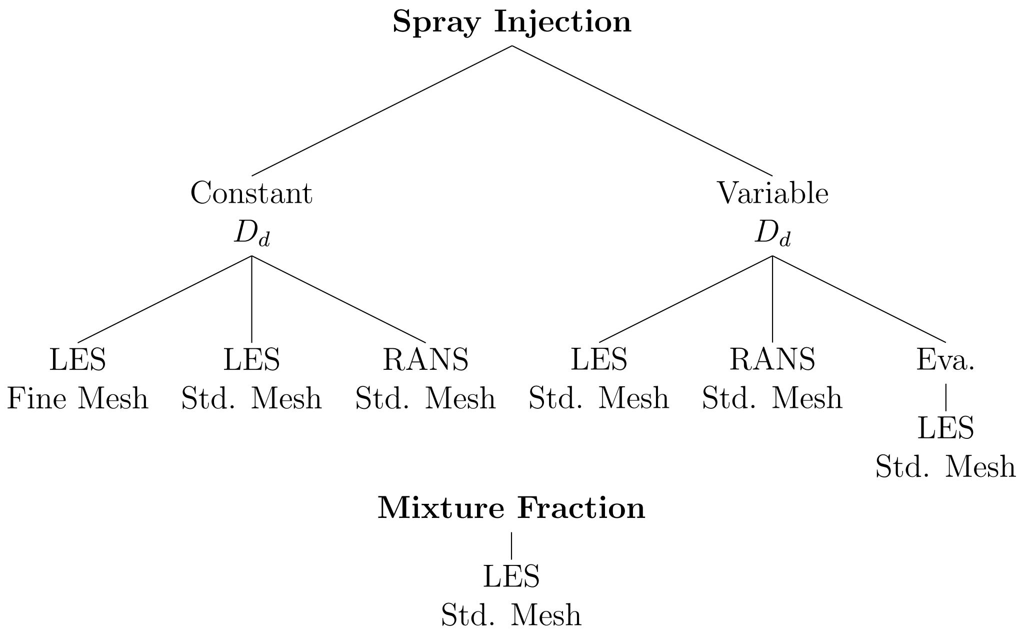

Figure 4.1: UCC simulations.

to analyze in detail the droplet dispersion and behavior inside the flow field created by the UCC. Varying the droplet size gives insight to the effect of buoyancy forces on spray dispersion, which is one of the main drivers of this experimental combustor. Evaporation is only included in one variable diameter simulation to explore the standard evaporation model in OpenFOAM. It is important to note that most of the simulations were carried out using a standard (std.) mesh, except one, the LES with constant D_d. Only one simulation with the fine mesh (see Fig. 4.2) was carried out due to the large computational time required from increasing the number of grid points.

In this work, CAD files were used to construct the computational meshes through Ansys' ICEM CFD [11] mesh generation software. Since the area of interest of the UCC is the main cavity, where fuel injection and combustion take place, the flow of the outer plenum is not modeled. This allows for a greater number of mesh points to be included in the main cavity and more flexibility in controlling the angled inlet velocities, which dictate the combustor's g-loading. Three unstructured tetrahedron meshes were created to solve for the flow and spray injection inside the UCC: standard and fine versions for the spray injection cases and a standard version for the mixture fraction case. Figure 4.2 shows the meshes used in this thesis and their corresponding number of grid points.

To increase the computational speed, MPI-based domain decomposition of the flow configuration is used and all of the simulations were carried out on 32-64 processors. All of the boundary conditions were matched as close as possible to the experimental conditions provided through private communication with Dr. David Blunck from the AFRL, who also provided fuel types and mass flow rates for the UCC. This section explains the geometry configuration and conditions used to model spray injection and mixture fraction.

4.2.1 Spray Injection

When simulating spray injection, only three out of the six fuel injectors were activated and a flow-deswirler was included in the outlet to match the experimental test set-up at the AFRL as shown in Fig. 4.3. The UCC's geometry, including the flow-deswirler, is shown in Fig. 4.4. It labels the main

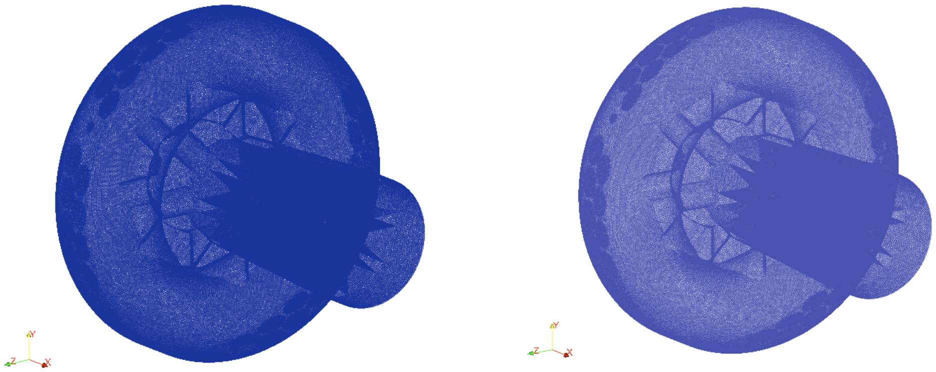

(a) Spray Fine (3,391,459 pts.)

(b) Spray Std. (973,392 pts.)

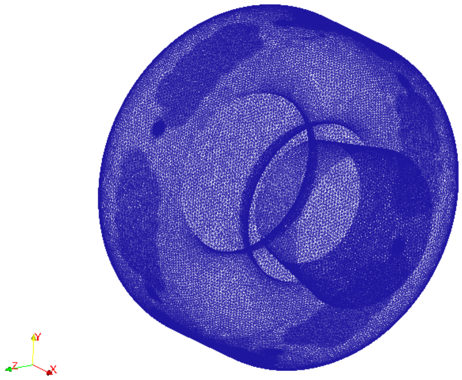

(c) Mixture Fraction Std. (848,940 pts.)

Figure 4.2: UCC simulation meshes

components of the UCC and the location of the fuel spray nozzles relative to the angled air jets. Figure 4.5 is a sectional view of the UCC at the plane of injection, which gives a better understanding of how the swirling motion is initialized. The blue arrows indicate the direction of the bulk air that the 45° air jets create, while the black arrows indicate the direction of fuel spray injection. The sprays inject liquid n-heptane normal to the main cavity towards the center and the angled air jets produce the circular bulk motion that creates three jet-in-crossflow scenarios. The spray injection results are divided into simulations with constant and variable droplet diameters. RANS and LES results were obtained for each. The main simulation conditions and parameters are listed in Table 4.1. In OpenFOAM, these are specified in the `sprayProperties` and `injectorProperties` files (see App. A).

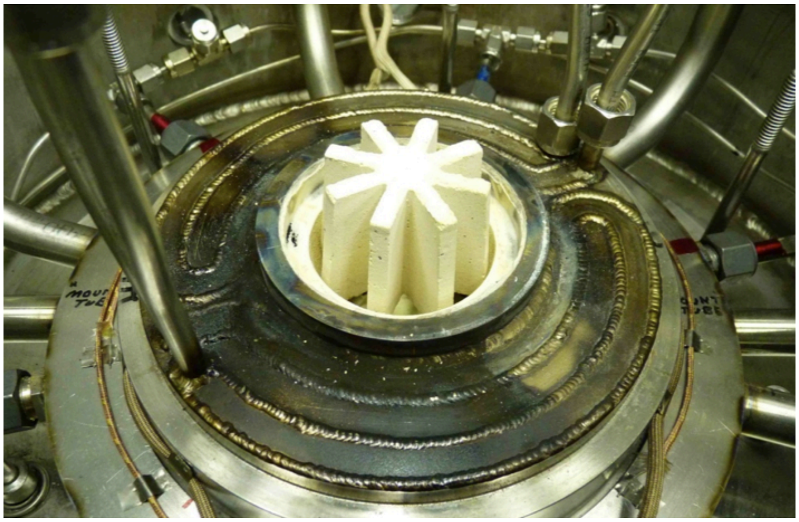

Figure 4.3: Experimental combustor with flow-deswirler installed.

In order to model the 45° angled air inlets, the `groovyBC` package was used. It allows to specify complex boundary conditions, and in this case it created a vectored boundary condition where the vector's magnitude and direction are specified. Each of the angled air inlets has a velocity magnitude of 2.5 m/s, which corresponds to a g-loading of 4.4 g as shown in Table 4.1. It was found that in order to achieve spray penetration with the given fuel rate, a low velocity for the angled air inlets was needed. Since the main topic

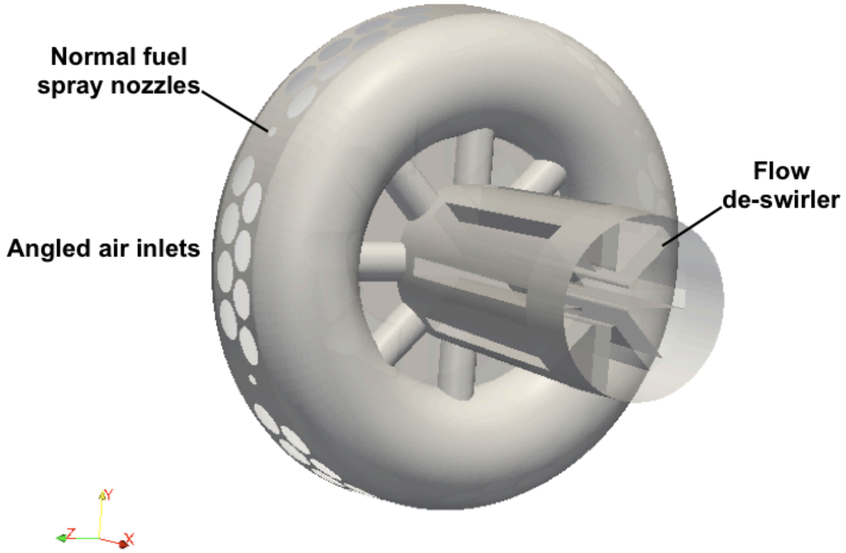

Figure 4.4: Spray injection combustor geometry.

of investigation was droplet dispersion at a Stokes number close to unity, a low g-loading was acceptable. N-heptane was chosen as the fuel because dieselFOAM was designed to model this fuel and a simple chemistry model is already implemented for future combustion modeling.

4.2.2 Mixture Fraction

When analyzing the fuel mixture fraction, the UCC's geometry was modified to a 40% length increase along the normal to the cavity center to increase the fuel's residence time as shown in Fig. 4.6. The flow de-swirler was removed and all of the 6 sprays inject propane gas, which are modeled as continuous fuel jets. This means that all of the fluids inside the UCC are in the gas phase, unlike the spray injection cases, which consist of a multiphase

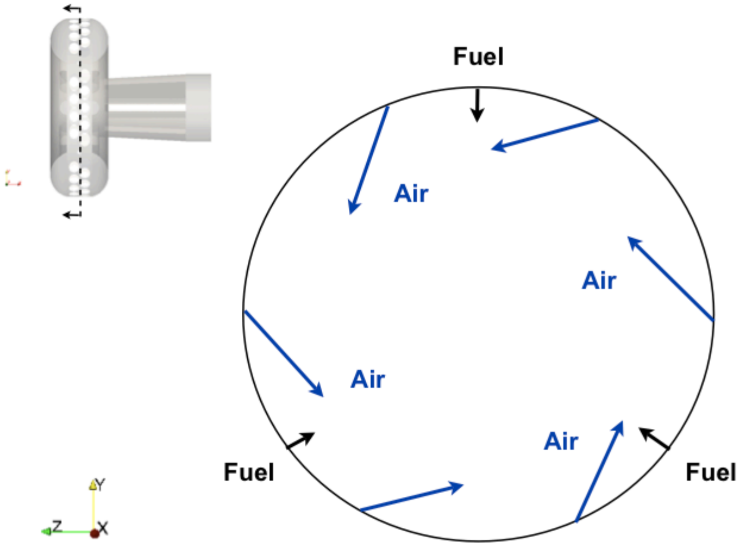

Figure 4.5: Sectional view of the combustor for spray injection configuration.

system. Therefore, the only differences between the mixture fraction and the spray configurations are the UCC's axial length, the incorporation of a flow-deswirler, the type and state of the fuel injected, and the number of fuel inlets used. Figure 4.7 is a sectional view of the UCC at the plane of injection, which shows the fuel and air inlet configuration.

All of the fuel inlets inject the gaseous fuel and the same swirling motion is generated by the angled air inlets like in the spray injection case. Table 4.2 lists the main conditions and parameters used to carry out the simulation. In contrast to the spray injection cases, a g-loading of 170 g is achieved due to the much higher air inlets' velocity. This g-loading was chosen because it is in the range of the combustor's operational condition once the majority of the fuel has been evaporated. The nozzle diameter had to be increased from its

Table 4.1: Spray simulations conditions.

	Constant $\mathbf{D_d}$	**Variable $\mathbf{D_d}$**
D_d (m)	7.5×10^{-5}	Variable
D_{nozzle} (m)	7.5×10^{-4}	7.5×10^{-4}
PDF	Uniform	Rosin Rammler $D_d^m = 7.5 \times 10^{-5}$ m $n = 3$
Parcels	500	500
C_d	0.9	0.9
St	0.9	0.9
Fuel type	liquid n-heptane	liquid n-heptane
# of sprays	3	3
Spray angle (deg)	85	85
Total $\dot{m}_{spr}$ (kg/m^3)	1.2×10^{-3}	1.2×10^{-3}
Total $\dot{m}_{air}$ (kg/m^3)	0.02	0.02
U_{spr} (m/s)	1.52	1.52
U_{air} (m/s)	2.5	2.5
G-loading (g)	4.4	4.4
T (K)	300	300
P (kPa)	101	101

spray counterpart in order to maintain the fuel flow velocity below supersonic, while maintaining the desired momentum ratio between the fuel and air inlets.

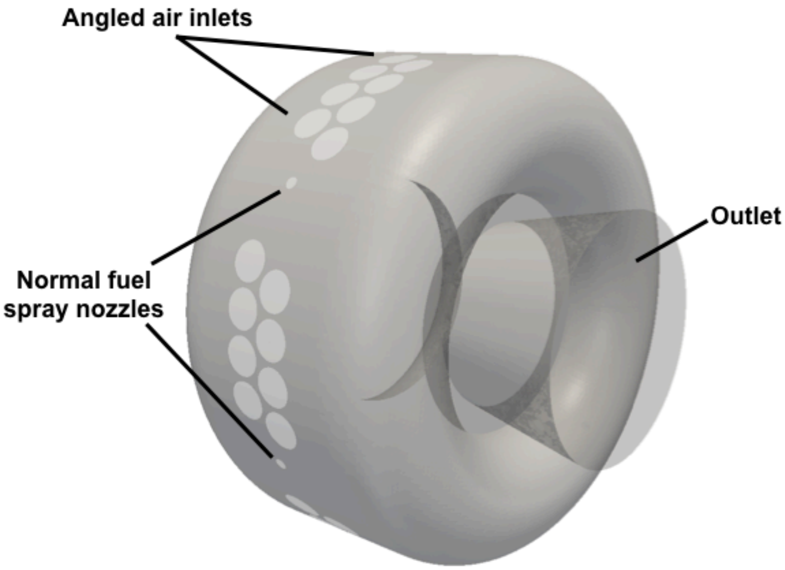

Figure 4.6: Gaseous phase combustor geometry.

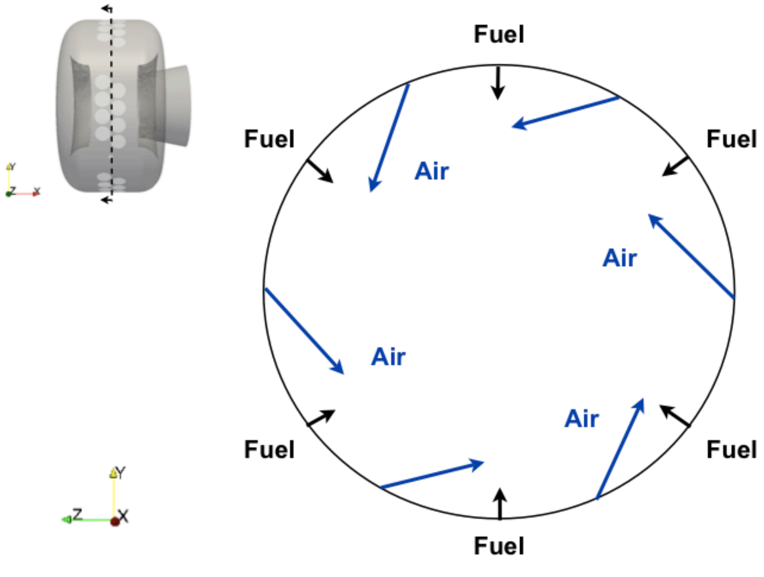

Figure 4.7: Sectional view of the combustor for mixture fraction configuration.

Table 4.2: Mixture fraction simulation conditions.

D_{nozzle} (m)	3.175×10^{-3}
Fuel type	propane gas
# of sprays	6
Total $\dot{m}_{spr}$ (kg/m^3)	1.79×10^{-3}
Total $\dot{m}_{air}$ (kg/m^3)	0.085
U_{spr} (m/s)	20
U_{air} (m/s)	15
G-loading (g)	170
T (K)	300
P (kPa)	101

Chapter 5

Results and Discussion

The results of this investigation are based on the simulations described in (4.2) and the conditions listed in Tables 4.1 and 4.2. They were carried out to investigate the flow inside the UCC and analyze droplet and gaseous fuel dispersion in the pre-combustion stage. These results are divided into the two main categories pertaining to this study, spray injection and mixture fraction. The spray injection results are further subdivided into constant and variable droplet size results.

5.1 Spray Injection

5.1.1 Constant droplet size

The main objective of maintaining the droplet size constant is to analyze droplet dispersion and understand the interaction of the turbulent flow with the spray inside the combustor. This is helpful in understanding the distribution of spray droplets prior to evaporation, providing a rough estimate of the combustion's ability to uniformly disperse fuel. It is then very important to have a flow field solution that resolves the majority of the highest energy containing scales, which in this case is the LES solution. In the discussion of results provided here, only instantaneous images of the flow fields are considered. It is found that the time-averaged profile did not provide additional insights in the context of the discussion below. Before arriving to a high resolution LES solution, RANS simulations with the standard mesh were performed, which will be compared to the fine mesh and standard mesh LES solutions (Figs.4.2a and 4.2c).

LES quality is tightly correlated to mesh density, so naturally the case with the fine mesh resulted in the most detailed flow structures as shown in Figs. 5.1 and 5.2. They are instantaneous flow fields at one flow trough time at UCC's center, while Fig. 5.2b is an isometric 3-D clipped view. They show the counter-clockwise circular flow due to the angled air inlets, which creates the expected swirling motion of the bulk flow concentrated at the center core of the UCC. The flow then accelerates over the front edges of the deswirler and finally exits through the outlet. Fig. 5.1 shows sharp velocity gradients in between each of the 8 sets of angled air inlets as the flow curves into full circular motion and at the inner core, which is a strong indication of turbulent flow structures. This is very important because these are signs of potential enhanced mixing due to turbulence at the areas of fuel injection, where the thorough mixing of reactants is imperative. The most interesting fact in this figure is the high velocity inner ring at the core, which contains velocity magnitudes as high as 4 times the injected air velocity. This high velocity ring is seen in more detail in Fig. 5.3, which shows a tangential velocity contour. It shows that the core where most of the uniform circular motion occurs is divided into an outer ring, at about 3.5 cm from the center, and an inner ring, at approximately 1.75 cm from the center. Also, the tangential velocity almost doubles radially inward at each of the rings, starting from the initial injected velocity.

Figure 5.4 is a velocity plot along the radius of the UCC shown in Fig. 5.3. It shows that the tangential velocity values correlate with the velocity magnitude from the outer radius of 7 cm until about 1.25 cm, which is the boundary of the inner high velocity ring. This means that most of the velocity up until the inner core ring is tangential velocity, almost full circular motion. Once the flow escapes the high velocity inner ring, a drastic drop in velocity occurs as shown in Fig. 5.4 and then a slight increase. This is probably due to the flow turning from a circular to an axial trajectory as it exits to the deswirler and finally the outlet.

In order to further understand the evolution of the flow, quantities pertaining to the subfilter turbulent flow are shown in Fig. 5.5. The subfilter kinetic energy or the residual kinetic energy is modeled based on the effective kinematic viscosity and the local strain rate.

$$K_r = \nu_{eff} |\widetilde{\mathbf{S}} \delta|. \tag{5.1}$$

They show that the majority of the velocity gradients and energy are concentrated inside the inner ring and at the fuel injection points. The strain rate contour shows that the highest velocity gradients occur inside the inner ring, but moderately high gradients occur at the fuel injection points as well, which adds evidence to the fact that turbulent mixing occurs in these areas. The residual kinetic energy plot shows a concentration of energy at the inner ring, which translates to a region well suited for the transport of burned cases to the outlet.

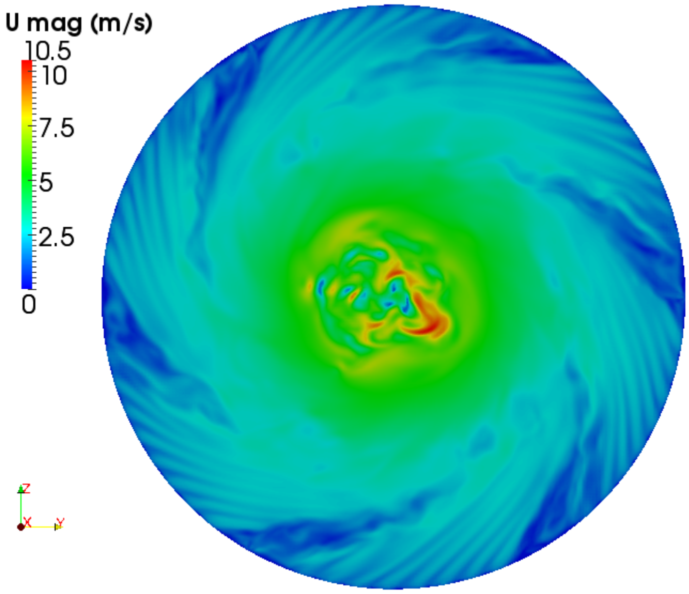

Figure 5.1: Instantaneous contour of velocity magnitude plotted along the plane of fuel injection.

The next step is to analyze the spray droplet dispersion due to this turbulent flow field. Figs. 5.6a and 5.6b are 3-D graphics of the instantaneous droplet dispersion inside the UCC at one flow through time. They show the three sprays in JICF configurations that gradually evolve from slightly turbulent at the point of injection to fully turbulent at the UCC's half radius, and finally break down at their tail by the swirling motion. This signals that the majority of the enhanced mixing occurs at the half radius, which is the outer boundary of the core's outer ring in Fig. 5.1. Another interesting observation

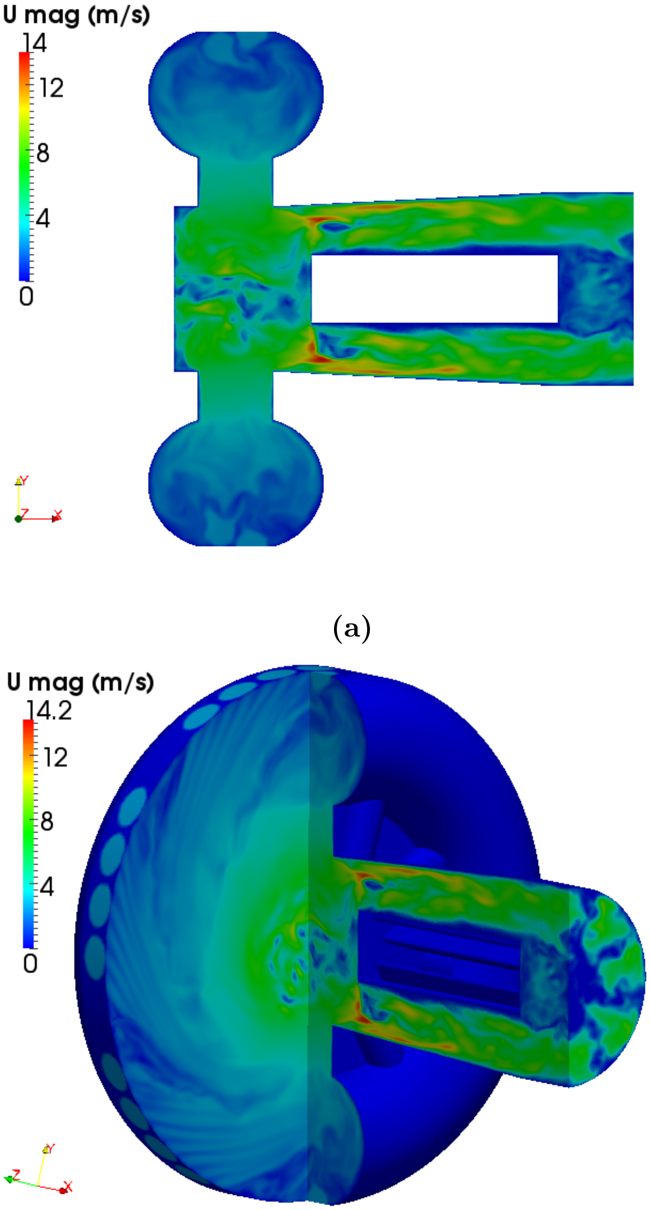

(a)

(b)

Figure 5.2: (a) Instantaneous velocity magnitude contour plotted along the axial centerline; (b) Instantaneous velocity magnitude 3-D contour plot clipped at the center point.

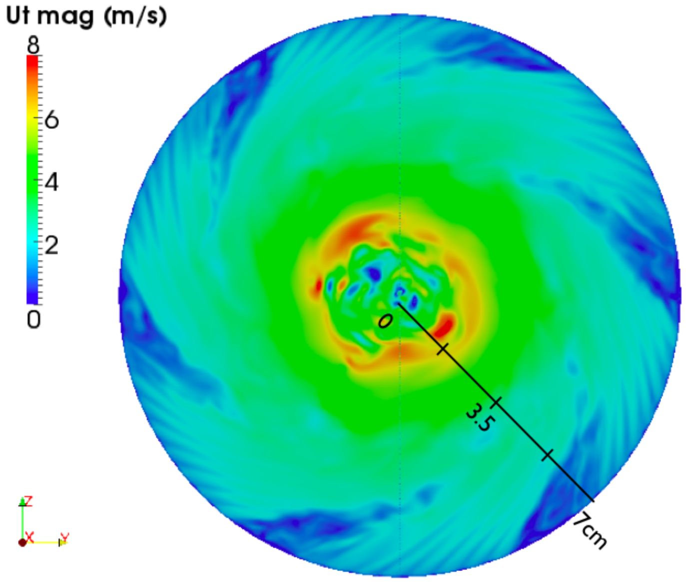

Figure 5.3: Instantaneous contour of tangential velocity plotted along the plane of fuel injection.

is that the high velocity inner ring acts as a shield that entrains the droplets in circular motion, allowing very few to escape into the axial flow. The lack of momentum for the droplets to escape the inner ring signals that the transport of burned gases and combustion products into the outlet might be severely affected. Finally, Fig. 5.6a shows droplet entrainment for each spray, which if significant and can cause unburned combustion products to not recirculate into the core flow. This may be attributed to the droplets' Stokes number being closed to unity, which would lead to the formation of high number density local pockets of spray droplets observed by Reveillon and Demoulin (2006).

Figures 5.7 and 5.8 are the velocity contour plots and 3-D droplet dis-

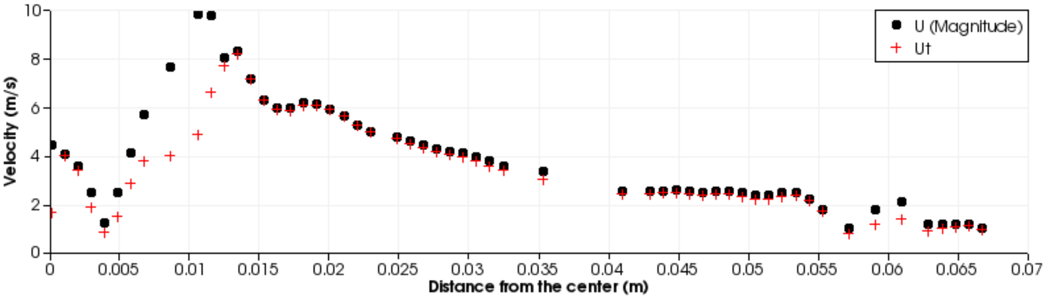

Figure 5.4: Velocity values plotted along the radius shown in Fig. 5.3.

persion graphics for the LES and RANS simulations with the standard mesh, respectively. The plots were captured at one flow through time as well and all of the same spray properties were maintained. The instantaneous velocity magnitude contour plots show that the flow structures are not as distinct as in the previous LES simulation and the RANS simulation shows no structures at all. The overall physics of the flow is maintained, but the inner ring is lost in the RANS simulation whereas the LES still exhibits this feature. This is due to the turbulence models used in the RANS calculations that are not suitable for flows with large swirling motion, which cause the flow to appear more diffused when compared to LES. The droplet dispersion figures in Fig. 5.7 are much more chaotic than the RANS counterpart in Fig. 5.8, where the droplets follow a very uniform trajectory towards the UCC's core. Overall, mesh density was a strong driver when trying to resolve the detailed flow structures that characterize a proper LES solution.

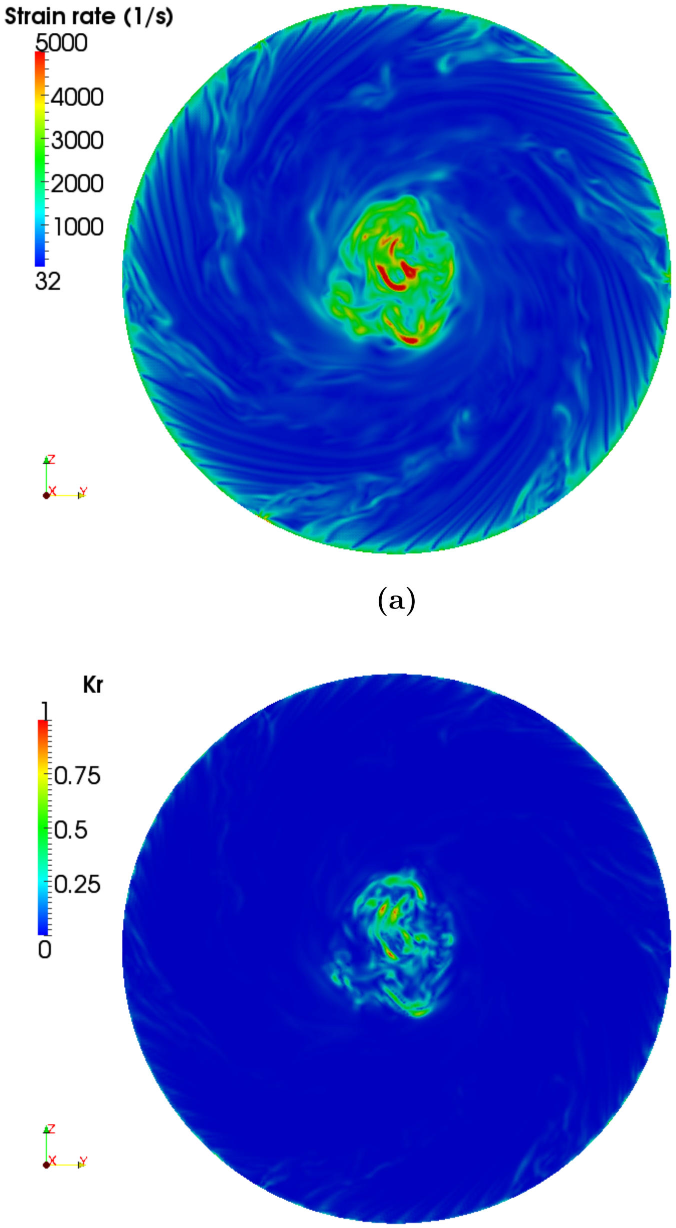

(a)

(b)

Figure 5.5: Contours of (a) strain rate and (b) residual kinetic energy plotted along the plane of fuel injection.

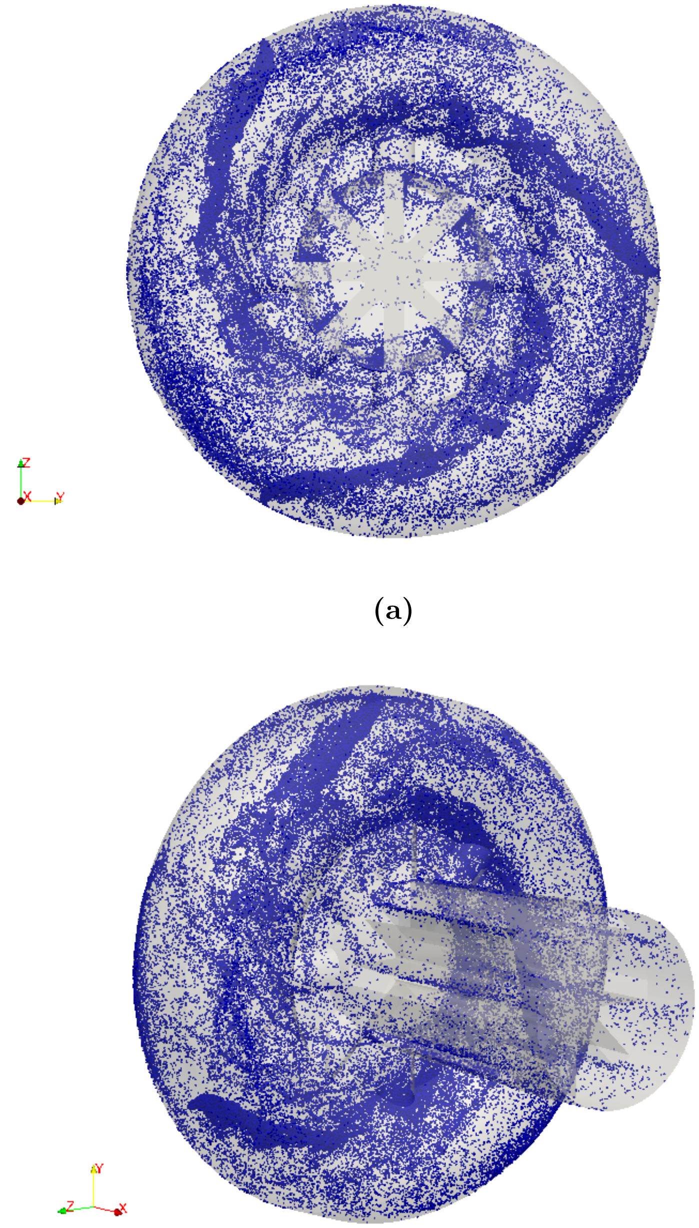

(a)

(b)

Figure 5.6: (a) Frontal and (b) isometric views of droplet dispersion for LES with fine mesh.

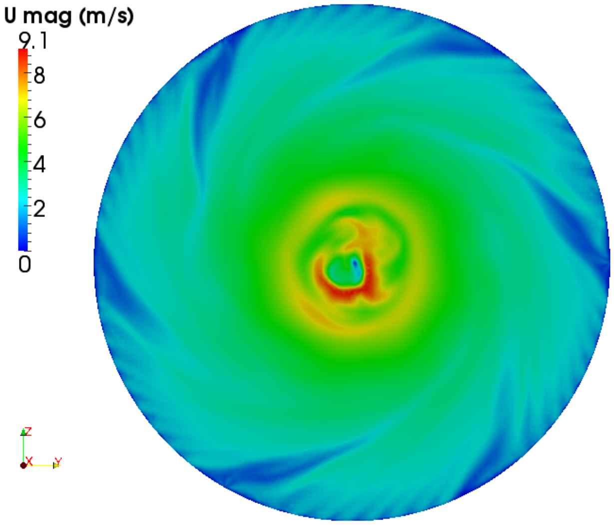

(a) Velocity contour plotted along the plane of fuel injection.

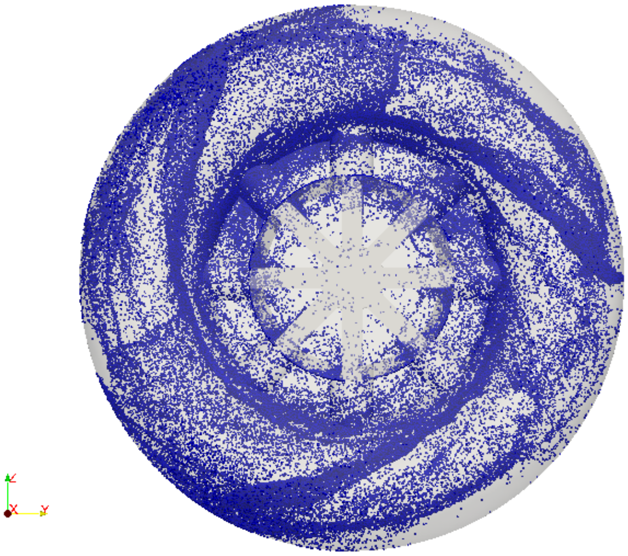

(b) Frontal view of droplet dispersion.

Figure 5.7: LES simulation with standard mesh.

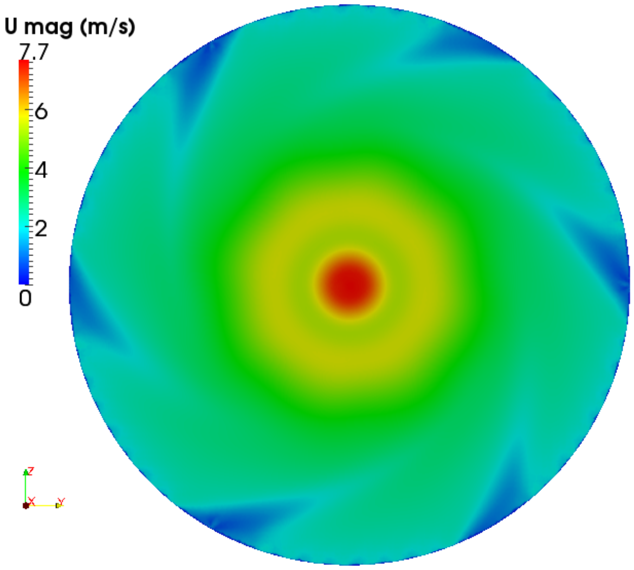

(a) Velocity contour plotted along the plane of fuel injection.

(b) Frontal view of droplet dispersion.

Figure 5.8: RANS with standard mesh

5.1.2 Variable droplet size

In order to obtain a greater understanding of the effect of buoyancy force inside the UCC, LES and RANS simulations were conducted with the fuel sprays injecting droplets with a variable diameter. The instantaneous LES and RANS results are shown in Fig. 5.9. They are droplet dispersion frontal views at one flow through time colored by droplet diameter. As expected, the droplet dispersion on the RANS simulation is very steady and uniform, whereas the LES is more chaotic due to the more resolved turbulent behavior. LES shows a smaller inner ring than the RANS simulation where very few droplets are present. This is due to the less diffused flow solution achieved by LES, which resolves the high velocity inner ring much better than the RANS' results. The main observation from these results is that the smaller droplets concentrate at the UCC's inner core, while the large droplets tend to move outward towards the rim of the combustor. This correlates with the UCC's purpose of having buoyancy forces drive the less dense burned combustion products into the center and towards the outlet, while keeping the denser unburned products re-circulating inside the UCC to complete combustion.

Once the injected droplets enter the combustor, evaporation starts to release the fuel into the gas phase. Based on OpenFOAM's standard evaporation method, Fig. 5.10 is an instantaneous contour of fuel fraction showing the unevaporated spray droplets in black. It shows that the evaporated fuel follows the expected swirling trajectory towards the center core. It also shows higher n-heptane concentration at the inner-most droplet gaseous fuel inter-

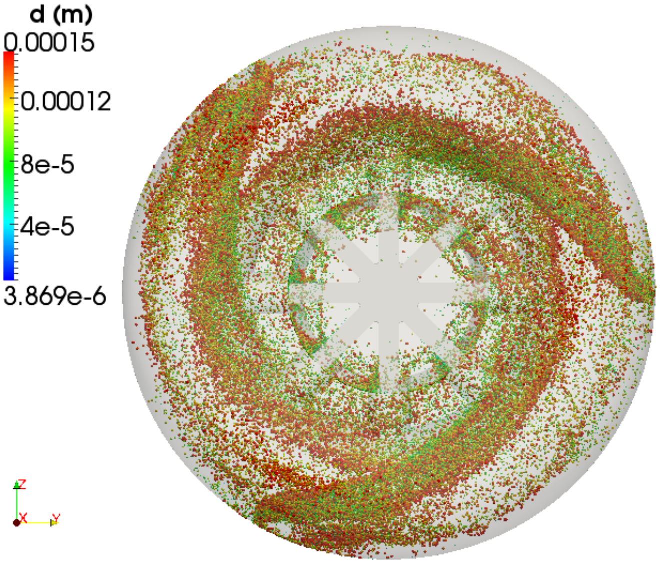

(a)

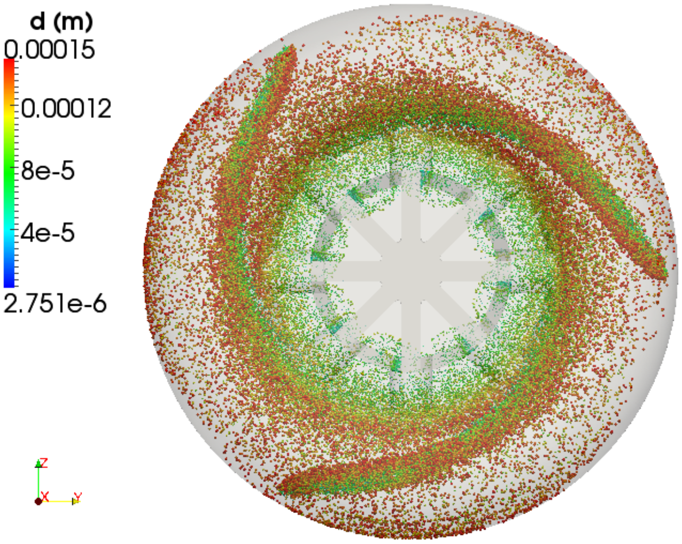

(b)

Figure 5.9: Instantaneous frontal views of droplet dispersion colored by droplet diameter for (a) LES and (b) RANS simulations

face, which means these are gaseous fuel saturated areas with higher droplet density.

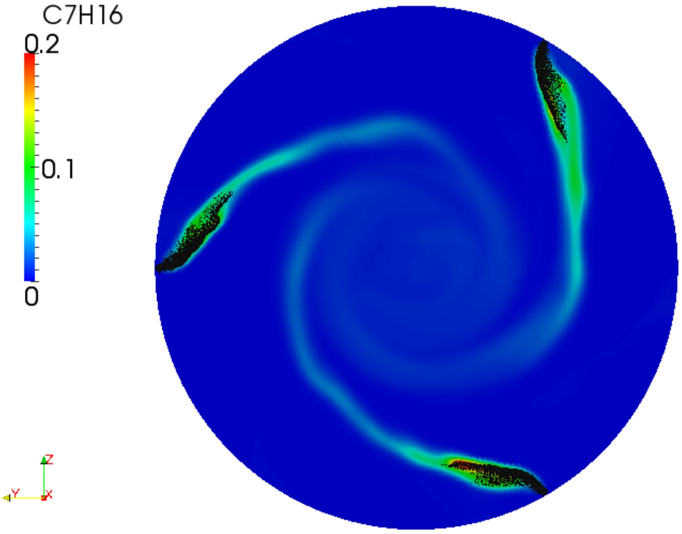

Figure 5.10: Instantaneous contour of fuel fraction with spray droplets plotted along the plane of fuel injection

5.2 Mixture Fraction

When analyzing fuel mixture fraction, only one LES was carried out to explore the gaseous fuel dispersion at a relatively high g-loading. Figure 5.11 shows the instantaneous flow field, while Fig. 5.12 shows the mixture fraction field inside the high-g combustor. The fuel injection inside the cavity is located in such a way that the air entering the cavity directly interacts with the fuel jet. In Fig. 5.12, it can be seen that the air injection deflects the fuel jet leading to a typical jet-in-crossflow type breakdown of the core. In addition, the angled air inlet in the cavity sets up a counter-clockwise rotation, which causes fuel circulation and mixing. The fuel jets do not interact directly, which could lead to additional instabilities in a reacting flow environment. There is some fuel re-circulation aft of every fuel jet when seen as a jet-in-crossflow, which can enhance the air-fuel mixing. Fig. 5.11 shows the high velocity inner ring that appears in the spray injection case with velocity magnitudes almost 3 times the injected velocity. This causes a barrier that may enhance mixing at the edge, but may cause the post-combustion removal of hot gases along the normal to the cavity center more difficult.

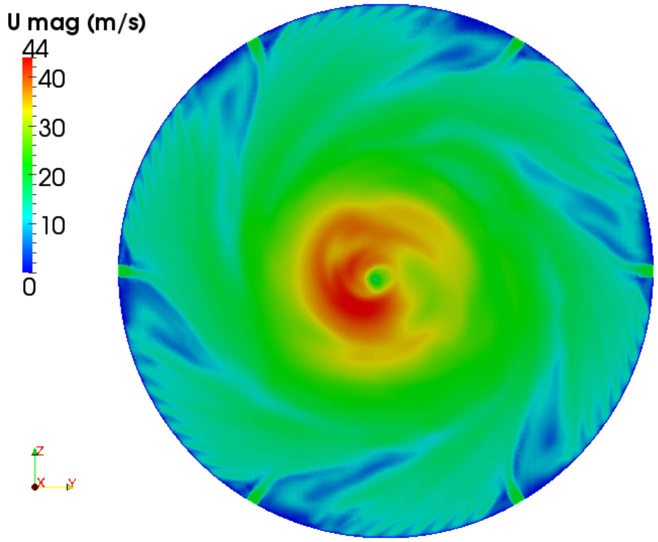

Figure 5.11: Instantaneous contour of velocity magnitude plotted along the plane of fuel injection

Further analysis on the flow is done by calculating subfilter turbulent

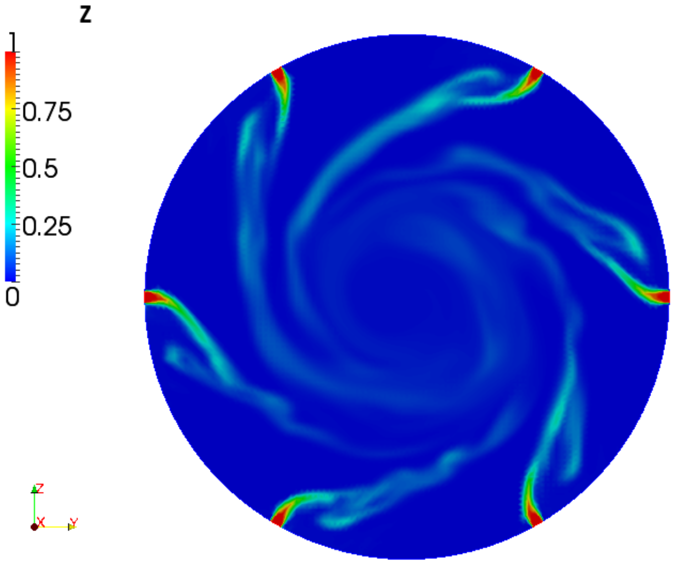

Figure 5.12: Instantaneous contour of mixture fraction plotted along the plane of fuel injection

flow quantities shown in Fig. 5.13. The effective viscosity is the sum of the laminar viscosity and the turbulent viscosity obtained from the Smagorinsky closure for the residual stress terms (Eq. 2.21). It is seen that the subfilter viscosity is concentrated along the fuel trajectory and has peak values both at the fuel injection ports and at the core. The subfilter kinetic energy shows peak values at the same locations, corresponding to shear-generated turbulence at the interface of the fuel jets with the surrounding swirling air. Further, kinetic energy patterns show increased turbulent intensity along the edge of the fuel jets, indicating strong interaction between the turbulent flow and the fuel jet, which is essential for the fast breakdown of the large scale scalar structures.

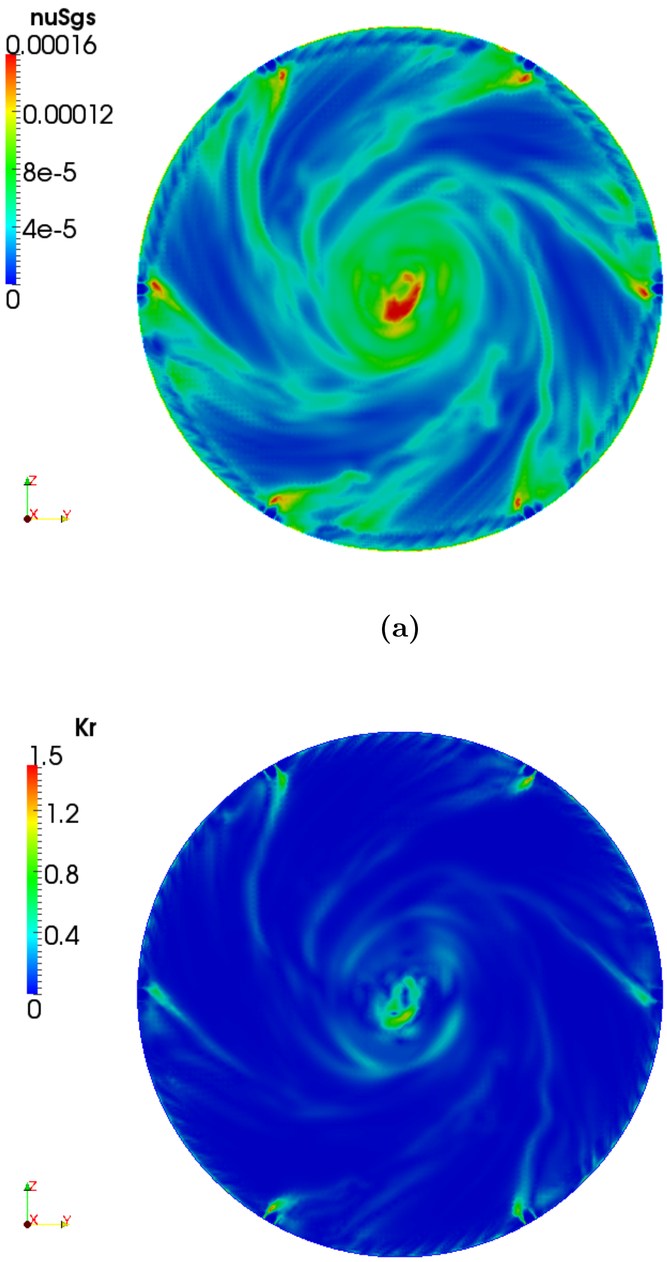

(a)

(b)

Figure 5.13: Contours of (a) turbulent viscosity and (b) residual kinetic energy plotted along the plane of fuel injection

The mixing process itself is better quantified through strain and scalar dissipation rates. The total scalar dissipation rate for the scalar is modeled as [23]:

$$\widetilde{\chi} = 2(D + D_T)\left(\frac{\partial \widetilde{Z}}{\partial \mathbf{x}}\right)^2 . \tag{5.2}$$

Figure 5.14 shows the strain rate and dissipation rates for the flow field discussed above. The main difference between an axial combustor and the cavity-based combustor is seen in the distribution of strain and dissipation rates. In conventional combustors, the strain rates are typically co-located with the dissipation rates. Note that dissipation rates are the highest at the fuel-air interface. Since these interfaces typically coincide with the inlet streams in a conventional combustors, the shear layers will evolve similar to the scalar mixing layers. In the UCC, the strain rates and dissipation rates are not necessarily co-located. For instance, Fig. 5.14a shows that the highest strain rates inside the cavity are located around the air jets and at the cavity's center. While the fuel jet does introduce some shear, the mass flow rate of the fuel jet is low compared to the air flow rate. Consequently, the dominant strain rates arise from the interaction of the air stream with the circulating flow inside the cavity. Similarly, the breakdown of the fuel jet is induced by the swirling flow inside the cavity. In a reacting case, this swirling mass will consist of burnt gases. Although the breakdown of the jet entails physics similar to a conventional jet in crossflow, the mixing induced by this breakdown occurs between the fuel and partially-burnt gases.

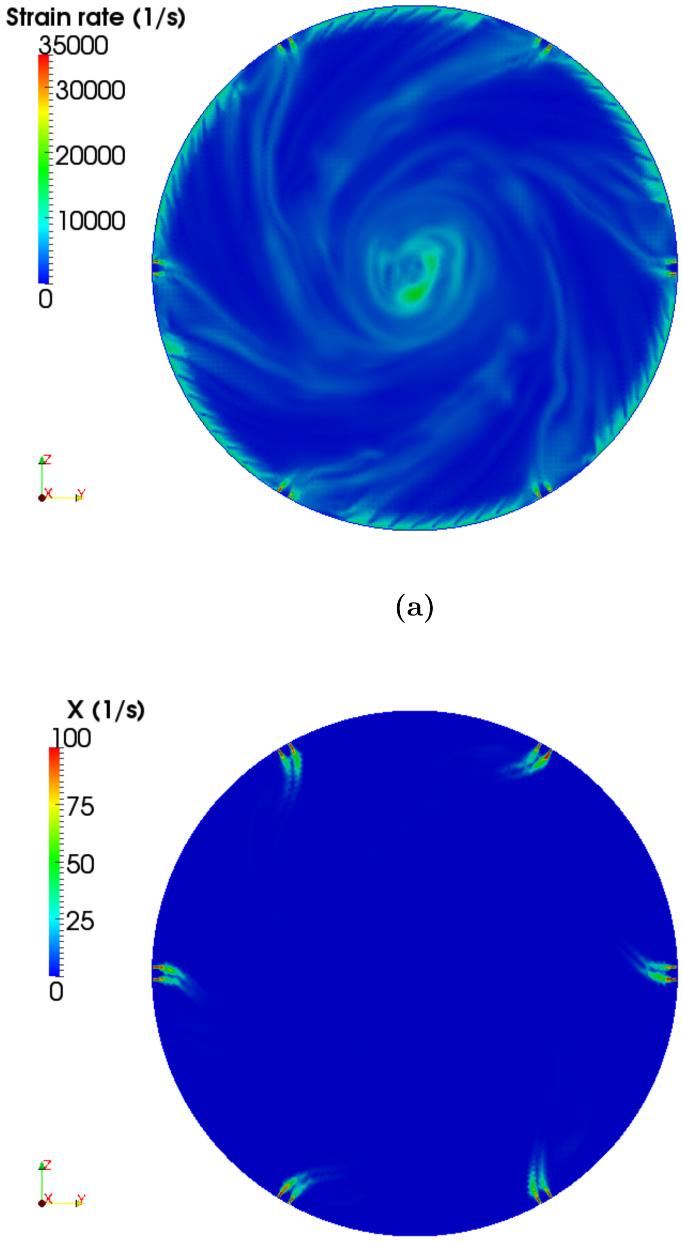

(a)

(b)

Figure 5.14: Contours of (a) strain and (b) dissipation rates plotted along the plane of fuel injection

Chapter 6

Conclusions

The flow inside a model high-g combustor was simulated using the LES and RANS modeling approaches. The spray injection of both non-evaporating and evaporating droplets was simulated to gain insight on fuel droplet dispersion inside the cavity. A passive scalar was tracked to study the gaseous fuel behavior. The computations reveal that the flow inside the cavity consists of a main swirling flow generated by the injection of the air stream from the plenum at a pitched angle. The fuel jets, located further away from the air stream injection holes, issue into the circulating flow and are deflected similar to a jet-in-crossflow configuration. The fuel jet breaks down and mixes with the circulating flow, which in a combusting environment will consist of burnt and partiallly-burnt gases. A high velocity vortex-like ring develops at the center core of the high-g combustor, which has enough momentum to potentially entrap the combustion products and decrease their flow into the outlet. The non-evaporating droplet simulations showed the presence of favorable turbulent regions at mid-radius that can enhance the mixing of reactants. Also, small droplet segregation zones appear fore of the spray injection points, which may increase in size as the flow develops further.

Droplet evaporation was significantly rapid, leading to a total liquid phase depletion very close to the injection region. The dispersion of fuel from these droplets showed interesting patterns. The fuel was found to mix close to the combustor core, which is also the region of flame location. Consequently, there is expected to be a strong interaction between turbulence-driven fuel dispersion and turbulence-enhanced mixing and combustion. Since the flow configuration promotes the mixing of pure oxidizer and fuel with burnt products, combustion models for this geometry should be able to handle the partially-premixed region explicitly. Further, the separation between regions of high strain rate and scalar dissipation rate implies that equilibrium models used to relate mixing time scales to turbulence time scales may not be valid in this flow.

Appendices

Appendix A

dieselFoam Main Input Files

A.1 `fvSchemes`

```
ddtSchemes
{
    default          Euler;
}

gradSchemes
{
    default          Gauss linear;
    grad(p)          Gauss linear;
}

divSchemes
{
    default          none;
    div(phi,rho)     Gauss limitedLinear 1;
    div(phi,U)       Gauss limitedLinearV 1;
    div(phiU,p)      Gauss linear;
    div(phi,k)       Gauss limitedLinear 1;
    div(phi,epsilon) Gauss limitedLinear 1;
    div(phi,Yi_h)    Gauss upwind;
    div(phi,fu_ft_h) Gauss multivariateSelection
    {
        fu limitedLinear 1;
        ft limitedLinear 1;
        hs limitedLinear 1;
    };
    div((muEff*dev2(grad(U).T()))) Gauss linear;
}

laplacianSchemes
{
    default          Gauss linear uncorrected;
    laplacian(muEff,U) Gauss linear uncorrected;
    laplacian(muEff,ft) Gauss linear uncorrected;
    laplacian(muEff,fu) Gauss linear uncorrected;
    laplacian(((alphah*mut)+alpha),hs) Gauss linear uncorrected;
    laplacian((rho|A(U)),p) Gauss linear uncorrected;
    laplacian(rhoD,k) Gauss linear uncorrected;
    laplacian(rhoD,epsilon) Gauss linear uncorrected;
}

interpolationSchemes
{
    default          linear;
    interpolate(HbyA) linear;
}

snGradSchemes
{
    default          corrected;
}

fluxRequired
{
    default          no;
    p;
```

```
}
```

A.2 fvSolution

```
solvers
{
    p
    {
        solver          PCG;
        preconditioner  DIC;
        tolerance       1e-09;
        relTol          0.1;
    }

    rho
    {
        $p;
        tolerance       1e-06;
    }

    "(U|Yi|hs|k|epsilon)"
    {
        solver          PBiCG;
        preconditioner  DILU;
        tolerance       1e-06;
        relTol          0.1;
    }
}

PISO
{
    nCorrectors      1;
    nNonOrthogonalCorrectors 2;
}
```

A.3 sprayProperties

```
interpolationSchemes
{
    U                cellPointFace;
    rho              cell;
    p                cell;
    T                cell;
}

subCycles        2;
atomizationModel off;
includeOscillation yes;
breakupModel       off;
injectorModel    hollowConeInjector;
collisionModel   off;
evaporationModel off;
heatTransferModel RanzMarshall;
dispersionModel off;
dragModel        standardDragModel;
wallModel        reflect;

specConstAtomizationCoeffs
{
    dropletNozzleDiameterRatio ( 0.4 );
    sprayAngle       ( 10 );
}

TABCoeffs
{
    y0               0;
    yDot0            0;
    Cmu              10;
    Comega           8;
    WeCrit           12;
}
```

```
ETABCoeffs
{
    Cmu             10;
    Comega          8;
    WeCrit          12;
    k1              0.2;
    k2              0.2;
    WeTransition    100;
}
ReitzDiwakarCoeffs
{
    Cbag            6;
    Cb              0.785;
    Cstrip          0.5;
    Cs              10;
}

ReitzKHRTCoeffs
{
    B0              0.61;
    B1              40;
    Ctau            1;
    CRT             0.1;
    msLimit         0.2;
    WeberLimit      6;
}

trajectoryCoeffs
{
    cSpace          1;
    cTime           0.3;
}

standardDragModelCoeffs
{
    preReFactor     0.166667;
    ReExponent      0.666667;
    ReLimiter       1000;
    CdLimiter       0.44;
    Cdistort        2.632;
}

standardEvaporationModelCoeffs
{
    evaporationScheme explicit;
    preReScFactor   0.6;
    ReExponent      0.5;
    ScExponent      0.333333;
}

RanzMarshallCoeffs
{
    preRePrFactor   0.6;
    ReExponent      0.5;
    PrExponent      0.333333;
}


hollowConeInjectorCoeffs
{
    dropletPDF
    {
        pdfType         RosinRammler;
        RosinRammlerPDF
        {
            minValue        1e-06;
            maxValue        0.00015;
            d               0.00015;
            n               3;
        }

        exponentialPDF
        {
            minValue        0.0001;
            maxValue        0.001;
            lambda          10000;
```

```
        }
    }

    innerConeAngle
        (0
         0
         0
        );

    outerConeAngle
        (
               85
               85
               85
         );
}

reflectCoeffs
{
    elasticity      0.9;
}
```

A.4 injectionProperties

```
(
    {
        injectorType        unitInjector;

        unitInjectorProps
        {
            position       (
                (-6.3416724e-007 0.067 -4.644e-005)
                (7.8809109e-008 -0.0332 0.0582)
                (-2.550591e-006 -0.0332 -0.0582)
                            );

            direction    (
                              ( 0 -1 0 )
                              ( 0 0.5 -0.86603 )
                              ( 0 0.5 0.86603 )
                                 );
            diameter        7.5e-4;
            Cd              0.9;
            mass            1.1745e-04;
            nParcels        500;

            X
            (
                1.0
            );

            massFlowRateProfile
            (
                (0 1e-8)
                (4.16667e-05 1e-6)
                (8.33333e-05 1e-5)
                (0.000125 0.0003915)
                (0.000166667 0.0003915)
                (0.000208333 0.0003915)
                (0.00025 0.0003915)
                (0.000291667 0.0003915)
                (0.000333333 0.0003915)
                (0.000375 0.0003915)
                (0.000416667 0.0003915)
                (0.000458333 0.0003915)
                (0.0005 0.0003915)
                (0.000541667 0.0003915)
                (0.000583333 0.0003915)
                (0.000625 0.0003915)
                (0.000666667 0.0003915)
                (0.000708333 0.0003915)
                (0.00075 0.0003915)
                (0.000791667 0.0003915)
                (0.000833333 0.0003915)
```

```
                (0.000875 0.0003915)
                (0.000916667 0.0003915)
                (0.000958333 0.0003915)
                (0.001 0.0003915)
                (0.00104167 0.0003915)
                (0.00108333 0.0003915)
                (0.001125 0.0003915)
                (0.00116667 0.0003915)
                (0.00120833 0.0003915)
                (0.05 0.0003915)
                (0.3 0.0003915)
            );

            temperatureProfile
            (
                (0.0      300)
                (0.05  300)
                (0.3  300)
            );
        }
    }
)
```

Appendix B

mixFoam Main Input Files

B.1 fvSchemes

```
ddtSchemes
{
    default          backward;
}

gradSchemes
{
    default          Gauss linear;
    grad(p)          Gauss linear;
    grad(U)          Gauss linear;
}

divSchemes
{
    default          none;
    div(U)           Gauss linear;
    div(phi,U)       Gauss linear;
    div(phi,nuTilda) Gauss limitedLinear 1;
    div((nuEff*dev(grad(U).T()))) Gauss linear;
    div((nuEff*dev2(grad(U).T()))) Gauss linear;
    div((nuEff*grad(Z))) Gauss linear;
    div(phi,Z)        Gauss limitedLinear01 1;
}

laplacianSchemes
{
    default          Gauss linear corrected;
    laplacian(nuEff,U) Gauss linear corrected;
    laplacian(nuEff,Z) Gauss linear corrected;
}

interpolationSchemes
{
    default          linear;
}

snGradSchemes
{
    default          corrected;
}

fluxRequired
{
    default          no;
    p                ;
}
```

B.2 fvSolution

```
solvers
{
    p
    {
        solver           PCG;
```

```
        preconditioner  DIC;
        tolerance       1e-06;
        relTol          0.1;
    }

"(U|nuTilda|Z)"
    {
        solver          PBiCG;
        preconditioner  DILU;
        tolerance       1e-06;
        relTol          0.1;
    }
}

PISO
{
    nCorrectors       1;
    nNonOrthogonalCorrectors 0;
}
```

B.3 ZEqn.H

```
{
    fvScalarMatrix ZEqn
    (
        fvm::ddt(Z)
      + fvm::div(phi,Z)
       -fvm::laplacian(turbulence->nuEff(), Z)
    );

    ZEqn.relax();
    ZEqn.solve();

    Info<< "Z␣␣min/max␣␣␣=␣" << min(Z).value() << ",␣"
        << max(Z).value() << endl;
}
```

Bibliography

[1] A.A. Amsden, P. J. O'Rourke, and T.D. Butler. Kiva-ii: A computer program for chemically reactive flows with sprays. *Los Alamos National Laboratory*, (LA-11560-MS), May 1989.

[2] W. S. Anderson, M. D. Polanka, J. Zelina, D. S. Evans, S. D. Stouffer, and G. R. Justinger. Effects of a reacting cross-stream on turbine film cooling. *Journal of Engineering for Gas Turbines and Power*, 132(5):051501, 2010.

[3] W. S. Anderson, J. T. Radtke, P. I. King, H. T., J. Zelina, and B. Sekar. Effects of main swirl direction on high-g combustion. In *44th AIAA/ASME/ SAE/ASEE Joint Propulsion Conference and Exhibit*, 2008.

[4] B. T. Bohan. Analysis of flow migration in an ultra-compact combustor. Master's thesis, Airforce Institute of Technology, 2011.

[5] A. Briones, B. Sekar, H. Thornburn, and J. Zelina. Effect of vane notch and ramp design on the performance of a rectangular inter-turbine burner. In *48th ASM Aerospace Sciences Meeting*, 2010.

[6] A. M. Briones, J. Zelina, and V. R. Katta. Flame stabilization in small cavities. *AIAA Journal*, 48:224–235, January 2010.

[7] D. George and Lewis. Combustion in a centrifugal-force field. *Symposium (International) on Combustion*, 13(1):625 – 629, 1971.

[8] D. George and Lewis. Centrifugal-force effects on combustion. *Symposium (International) on Combustion*, 14(1):413 – 419, 1973.

[9] M. Germano. Turbulence : The filtering approach. *Journal of Fluid Mechanics*, 286:229–255, 1991.

[10] R. Gjesing, J. Hattel, and U. Fritsching. Coupled atomization and spray modelling in the spray forming process using openfoam. *Engineering Applications of Computational Fluid Mechanics*, 3:471–486, 2009.

[11] ANSYS Inc. *ICEM CFD version 14.0.* 2011.

[12] H. Jasak, H. G. Weller, and N. Nordin. In-cylinder cfd simulation using a c++ object-oriented toolkit. *SAE International*, 2004.

[13] F. Kärrholm, F. Tao, and N. Nordin. Three-dimensional simulation of diesel spray ignition and flame lift-off using openfoam and kiva-3v cfd codes. *SAE International*, 2008.

[14] H. I. Kassem, K. M. Saqr, H. S. Aly, M. M. Sies, and M. A. Wahid. Implementation of the eddy dissipation model of turbulent non-premixed combustion in openfoam. *International Communications in Heat and Mass Transfer*, 2011.

[15] D. Kirk, G. Guenette, S. Lukachko, and I. Waitz. Gas turbine engine durability impacts of high fuel-air ratio combustors-part ll: Near-wall reaction effects on film-cooled heat transfer. *Journal of Engineering for Gas Turbines and Power*, 125:751–759, 2003.

[16] C. Kralj. *Numerical Simulation of Diesel Spray Processes.* PhD thesis, Imperial College, 1995.

[17] B. Launder and D. Spalding. *Mathematical Models of Turbulence.* London Academic Press, 1972.

[18] OpenCFD Ltd. *OpenFOAM version 1.7.1.* 2010.

[19] T. Lucchini, G. D'Errico, and N. Nordin. Cfd modelling of gasoline sprays. *SAE International*, 2005.

[20] N. Nordin. *Complex Chemistry Modeling of Diesel Spray Combustion.* PhD thesis, Chalmers University of Technology, 2001.

[21] R. Novella, A. Garcia, J.M. Pastor, and V. Domenech. The role of detailed chemical kinetics on cfd diesel spray ignition and combustion modelling. *Mathematical and Computer Modelling*, 2011.

[22] F. Peng and N. Nordin. Numerical investigation of mesh/turbulence/spray interaction for diesel applications. *SAE International*, 2005.

[23] C. D. Pierce and P. Moin. A dynamic model for subgrid-scale variance and dissipation rate of a conserved scalar. *Physics of Fluids*, 10:3041 – 3044, 1998.

[24] S. B. Pope. *Turbulent Flows.* Cambridge University Press, 2000.

[25] J. Reveillon and F.X. Demoulin. Evaporating droplets in turbulent reacting flows. *Proceedings of the Combustion Institute*, 2007(31):2319 – 2326, 2006.

[26] W. A. Sirignano. *Fluid Dynamics and Transport of Droplets and Sprays.* Cambridge University Press, 2010.

[27] H. J. Thornburg, B. Sekar, J. Zelina, C. Lin, and R. Holder. Prediction of inter-turbine burner (itb) performance with curved radial vane cavity at various equivalence ratios. *ASME Conference Proceedings*, 2008(43161):2131–2139, 2008.

[28] V. A. Vuorinen, H. Hillamo, O. Kaario, M. Nuutinen, M. Larmi, and L. Fuchs. Effect of droplet size and atomization on spray formation: A priori study using large-eddy simulation. *Flow, Turbulence, and Combustion*, 2011.

[29] L. Wang and M. R. Maxey. Settling velocity and concentration distribution of heavy particles in homogeneous isotropic turbulence. *Journal of Fluid Mechanics*, 256:27 –68, 1993.

[30] F. M. White. *Viscous Fluid Flow.* McGraw-Hill, 2006.

[31] J. Zelina, W. Anderson, P. Koch, and D. T. Shouse. Compact combustion systems using a combination of trapped vortex and high-g combustor technologies. *ASME Conference Proceedings*, (43130):1–9, 2008.

[32] J. Zelina, R. T. Greenwood, and D. T. Shouse. Operability and efficiency performance of ultra-compact, high gravity (g) combustor concepts. *ASME Conference Proceedings*, 2006(42363):87–95, 2006.

[33] J. Zelina, G. J. Sturgess, and D. T. Shouse. The behavior of an ultra-compact combustor (ucc) based on centrifugally-enhanced turbulent burning rates. *40th AIAA/ASME/SAE/ASEE Joint Propulsion Conference and Exhibit*, July 2004.

Vita

Jaime Martinez Guerrero was born in Estado de Mexico, Mexico on July 17 1987, the son of Jaime E. Martinez Rodriguez and Maria C. Guerrero de Martinez. He graduated as salutatorian from Robert E. Lee High School in Baytown, Texas. He received his Bachelor of Science in Aerospace Engineering from the University of Texas at Austin in May 2009. In August of 2010, he returned to the University of Texas at Austin and joined the Aerothermodynamics and Fluid Mechanics Master's program.

Permanent address: 4823 Bentonite Blvd
Baytown, Texas 77522

This thesis was typeset with LaTeX[†] by the author.

[†] LaTeX is a document preparation system developed by Leslie Lamport as a special version of Donald Knuth's TeX Program.